

Land–Water Boundary Treatment for a Tsunami Model With Dimensional Splitting

ELENA TOLKOVA¹

Abstract—The Method of Splitting Tsunamis (MOST) model adapted by National Oceanic and Atmospheric Administration (NOAA) for tsunami forecasting operations is praised for its computational efficiency, associated with the use of splitting technique. It will be shown, however, that splitting the computations between x and y directions results in specific sensitivity to the treatment of land–water boundary. Slight modification to the reflective boundary condition in MOST caused an appreciable difference in the results. This is demonstrated with simulations of the Tohoku-2011 tsunami from the source earthquake to Monterey Bay, California, and in southeast Alaska, followed by comparison with tide gage records. In the first case, the better representation of later waves (reflected from the coasts) by the modified model in a Pacific-wide simulation resulted in twice as long match between simulated and observed tsunami time histories at Monterey gage. In the second case, the modified model was able to propagate the tsunami wave and approach gage records at locations within narrow channels (Juneau, Ketchikan), to where MOST had difficulty propagating the wave. The modification was extended to include inundation computation. The resulting inundation algorithm (Cliffs) has been tested with the complete set of NOAA-recommended benchmark problems focused on inundation. The solutions are compared to the MOST solutions obtained with the version of the MOST model benchmarked for the National Tsunami Hazard Mitigation Program in 2011. In two tests, Cliffs and MOST results are very close, and in another two tests, the results are somewhat different. Very different regimes of generation/disposal of water by Cliffs and MOST inundation algorithms, which supposedly affected the benchmarking results, have been discussed.

Key words: Tsunamis, numerical modeling, dimensional splitting, reflective boundary, inundation, wave runup.

1. Introduction

Splitting a time-space hyperbolic problem into simpler subproblems to be solved independently, also known as a method of fractional steps, is a powerful

numerical technique widely applied in computational fluid dynamics (STRANG 1968; LEVEQUE 2002). In particular, the shallow-water equations (SWE) commonly used to describe tsunami evolution with respect to time and two space variables can be split into simpler one-dimensional (1D) problems describing wave propagation in either direction. The idea of the dimensional splitting is to obtain the solution of the original 2D problem by solving the 1D subproblems in an alternating manner. This arrangement is very efficient computationally and greatly simplifies the derivation of associated numerical routines. It also facilitates parallelization of the computations. A tsunami model taking advantage of the dimensional splitting is the Method Of Splitting Tsunamis (MOST) numerical model in use in the NOAA's Center for Tsunami Research (NCTR) (TITOV and GONZALEZ 1997; TITOV *et al.* 2005).

It is not widely understood, however, that the splitting technique might require special attention to setting boundary conditions. LEVEQUE (2002, §17.9) demonstrated that determining boundary conditions needed for the fractional steps might be nontrivial, with an example of solving a 1D equation $q_t + uq_x = -\beta q$ split into $q_t + uq_x = 0$ and $q_t = -\beta q$. In that example, a constant inflow through an open boundary $q(0, t) = 1$ for the original equation had to be recalculated to a different value when used with the first subproblem.

This work originated with yet another unexpected effect associated with formulating solid wall (reflective) boundary conditions for the subproblems yielded by the dimensional splitting. We show that the dimensional splitting might result in underestimating an amplitude of a reflected wave in the MOST model, unless the reflecting boundary is aligned with either x or y coordinate axis.

The MOST model is based on the 1D algorithm VTCS-2 (TITOV and SYNOLAKIS 1995) combined with

Electronic supplementary material The online version of this article (doi:10.1007/s00024-014-0825-8) contains supplementary material, which is available to authorized users.

¹ NorthWest Research Associates, Bellevue, WA 98009-3027, USA. E-mail: e.tolkova@gmail.com; elena@nwra.com

the dimensional splitting (STRANG 1968; TITOV and SYNOLAKIS 1998). For its computational efficiency associated with the use of the splitting method, the model was adapted by National Oceanic and Atmospheric Administration (NOAA) for tsunami forecasting operations. Presently, the MOST model is incorporated into the Short-term Inundation Forecast of Tsunamis (SIFT) system, which also integrates real-time tsunami measurements, a basin-wide pre-computed database of water level and flow velocities for potential seismic unit sources, and sets of pre-tested high-resolution grids focusing on specific coastal locations. Once a synthetic low-resolution estimate of the tsunami wave in the deep ocean is deduced from the measurements, the MOST model is then used to provide high resolution tsunami inundation forecast for the aforementioned coastal locations in minutes of computational time per each (TANG *et al.* 2012). At the same time, as can be seen from the comparisons of modeled and tide-gauge data from recent tsunamis (see Event Pages at http://nctr.pmel.noaa.gov/database_devel.html), the model often under-estimates later waves.

This work starts with a brief overview of the VTCS-2 difference scheme. Formulations of the reflective boundary conditions are discussed in Sect. 3. The difference between the suggested reflection treatment and that given in TITOV and SYNOLAKIS (1995) is demonstrated in Sect. 4 with simulations of a wave propagating in a straight channel at an angle to coordinate axes, and under various real-world settings. The latter includes simulation of the Tohoku-2011 tsunami from the source earthquake to Monterey Bay, CA, and into fjords, bays, and inlets of southeastern Alaska, followed by comparison with tide gage records.

The proposed algorithm, named Cliffs, is generalized to efficiently handle land inundation (Sect. 5). The rest of the work (Sect. 6) presents testing Cliffs inundation algorithm with canonical benchmark problems: runup of a non-breaking and a breaking wave on a plane sloping beach (SYNOLAKIS 1987), runup on a conical island (BRIGGS *et al.* 1995), simulation of a wave-tank experiment with a scaled model of Monai Valley (LIU *et al.* 2008), and simulation of the Okushiri Island inundation in the 1993 Hokkaido tsunami (TAKAHASHI 1996). Cliffs

solutions to the benchmark problems are compared to the MOST solutions obtained with the version of the MOST model benchmarked for NTHMP in 2011 (TOLKOVA 2012). Given that the two models share the same propagation part, this comparative benchmarking provided a rare opportunity to observe variability in the results due to an inundation algorithm alone. Very different regimes of generation/removal of water and momentum by Cliffs and MOST inundation algorithms, which supposedly affected the benchmarking results, have been discussed.

2. Numerical Algorithm

The MOST numerical model solves the SWE given below in matrix notation in the Cartesian coordinates:

$$W_t = A(W)W_x + B(W)W_y + C(W) \quad (1)$$

where subscript denotes partial derivatives; $W = (h, u, v)^T$ is a vector of state variables; h is height of the water column; u, v are particle velocity components in x and y directions;

$$A = -\begin{pmatrix} u & h & 0 \\ g & u & 0 \\ 0 & 0 & u \end{pmatrix}, \quad B = -\begin{pmatrix} v & 0 & h \\ 0 & v & 0 \\ g & 0 & v \end{pmatrix}, \quad (2)$$

$$C = \begin{pmatrix} 0 \\ gd_x - a^x \\ gd_y - a^y \end{pmatrix}$$

g is acceleration due to gravity; $(a^x, a^y) = n^2 g \sqrt{u^2 + v^2} / h^{4/3} (u, v)$ are the components of acceleration due to friction in Manning formulation, n is Manning's roughness coefficient; d is undisturbed water depth, or vertical coordinate of sea bottom measured down from the mean sea level (MSL). Negative values of d correspond to dry land and give the land elevation relative to MSL. The SWE are solved by splitting into subsystems associated with a single space variable each:

$$W_t = A(W)W_x + C_1(W) \quad (3)$$

$$W_t = B(W)W_y + C_2(W) \quad (4)$$

where $C_1 = (0, gd_x - a^x, 0)^T$, $C_2 = (0, 0, gd_y - a^y)^T$.

Assume that linear difference operators S_x and S_y advance the solution of (3) and (4) respectively through a time step τ . Then the composite operator $S = S_y \cdot S_x$ advances the solution of the original system (1) through τ , and, since $AB \neq BA$, contributes a splitting error of order τ^2 in each step (STRANG 1968; LEVEQUE 2002). However, as discussed in LEVEQUE (2002), associated coefficients are small, and in many cases, switching to the second-order accurate Strang-type splitting schemes does not improve the results.

For the particular splitting (3)–(4) used in MOST, the subsystems have identical structure. Two equations with respect to (h, u) in (3) or with respect to (h, v) in (4) describe a wave propagation in 1D configuration in either x or y direction. The 1D problems are solved independently for each row and then for each column of a structured un-staggered grid. The remaining equation is present in the 2D case only and contributes to evolution of a velocity component orthogonal to the direction of computations. The discretization of equations (3)–(4) is described in TITOV and SYNOLAKIS (1995, 1998). Diffusive and dispersive properties of the VTCS-2/MOST numerical scheme in a basin with constant depth are investigated in BURWELL *et al.* (2007). For MOST equations in an arbitrary orthogonal coordinate systems (e.g. spherical), see BURWELL and TOLKOVA (2008). The VTCS-2 algorithm is briefly re-visited here and presented in a coding-friendly form.

On the example of system (3), the 1D propagation equations are re-written in terms of Riemann invariants

$$p = u + 2\sqrt{gh}, \quad q = u - 2\sqrt{gh}$$

and eigenvalues $\lambda_{1,2} = u \pm \sqrt{gh}$ as

$$p_t = -(\lambda_1 \cdot p_x - gd_x) - \alpha^x \quad (5)$$

$$q_t = -(\lambda_2 \cdot q_x - gd_x) - \alpha^x \quad (6)$$

The explicit forward difference scheme for non-uniform grid spacing to solve each characteristic equation is given below for p -invariant:

$$p_j^n = p_j^{n-1} - \frac{\Delta t}{\Delta x_j + \Delta x_{j-1}} \left[Q(j+1, j-1) + \frac{\lambda_j \Delta t}{\Delta x_{j-1}} Q(j, j-1) - \frac{\lambda_j \Delta t}{\Delta x_j} Q(j+1, j) \right] - \Delta t \alpha^x \quad (7)$$

where

$$Q(k, j) = \frac{1}{2}(\lambda_k + \lambda_j)(p_k - p_j) - g(d_k - d_j) \quad (8)$$

Δt is time increment; $\Delta x_j = x_{j+1} - x_j$ is space increment; all the right hand side variables are evaluated at a time step $n-1$. Term Q can be recognized as a counterpart of the expression in brackets on the right hand side of (5)–(6). In the steady state, $Q = 0$, which ensures an automatic preservation of steady state. The solver (7) is first-order accurate in time and second-order accurate in space. In a basin with constant depth, the scheme is stable under the known limit on the Courant number: $|\lambda| \Delta t / \Delta x \leq 1$.

Once values p and q have been updated, the corresponding state variables are recovered as

$$u = (p + q)/2 \quad (9)$$

$$h = (p - q)^2 / 16g \quad (10)$$

3. Handling Totally Reflective Boundary

VTCS-2/MOST algorithm does not use difference scheme (7) in wet nodes next to a reflective boundary (a vertical wall). Instead, an outgoing Riemann invariant in the last wet node is advanced from t_{n-1} to t_n using a two-point stencil, while the incoming invariant is specified as follows (TITOV and SYNOLAKIS 1995, 1998).

In a wet node on the right of the reflecting boundary, the incoming p -invariant at t_n is set to

$$p^n = -q^n. \quad (11)$$

For x -direction of computations, this procedure implies $u^n = 0$ at the edge node, which sets the reflective wall immediately in front of the wet node. Likewise, in a wet node on the left of the reflecting boundary, the incoming q -invariant is set to

$$q^n = -p^n, \quad (12)$$

which sets the reflective wall immediately behind the wet node, as depicted in Fig. 1.

Alternatively, a wet node next to a reflecting wall can still be treated as a wet node with both wet neighbors, by mirroring the wet area in the wall and reversing the direction of the normal velocity

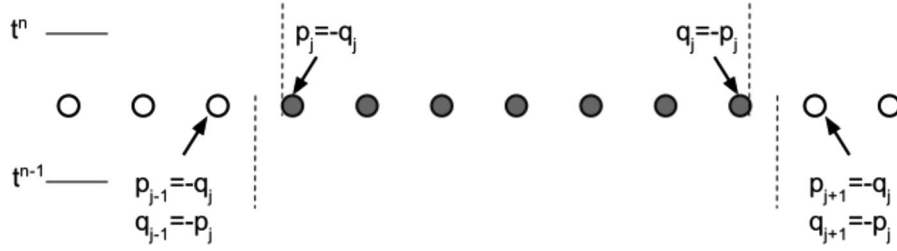


Figure 1

Dark circles water, white circles high-elevated land (vertical wall). Boundary treatment in MOST: $p = -q$ (right of the wall) or $q = -p$ (left of the wall), after the invariant propagating toward the wall has been updated. Boundary treatment in Cliffs: prior to updating the solution, the invariants are assigned in ghost cells. Dashed lines resulting location of reflecting boundaries in MOST (upper) and Cliffs (lower)

component (LEVEQUE 2002; SHI *et al.* 2012). Specifically, let j -th wet node be the last node in a wet segment bounded by a vertical wall on the right. A ghost ($j+1$) wet node is introduced, with $d_{j+1} = d_j$, $h_{j+1} = h_j$, $v_{j+1} = v_j$, $u_{j+1} = -u_j$, therefore $p_{j+1} = -u_j + 2\sqrt{gh_j} = -q_j$, $q_{j+1} = -u_j - 2\sqrt{gh_j} = -p_j$. The resulting boundary conditions in terms of Riemann invariants are:

$$p_{j+1} = -q_j, \quad q_{j+1} = -p_j, \quad v_{j+1} = v_j \quad (13)$$

on the right of j -th wet node, and

$$p_{j-1} = -q_j, \quad q_{j-1} = -p_j, \quad v_{j-1} = v_j \quad (14)$$

on the left of j -th wet node. Conditions (13)/(14) imposed in ghost nodes at t_{n-1} replace the conditions (11)/(12) imposed in edge wet nodes at t_n (see Fig. 1). This treatment sets the reflecting wall exactly in the middle between the neighboring wet and dry nodes. Also unlike (11) and (12), the new boundary conditions are obtained without making any assumptions about the direction of the characteristics.

Hereafter, the wetting–drying interface being described (that is, the suggested reflection formulation followed with an inundation algorithm in Sect. 5) will be referred to as Cliffs. MOST reflection and/or wetting–drying algorithm refers to the algorithms in the MOST model presently used in PMEL, which are mainly (but not entirely) those of the VTCS-2 1D model.

4. How Much Difference Does it Make?

So far, the only recognized advantage of the ‘ghost cells’ approach has been an option to keep the

same numerical stencil throughout, avoiding the need to switch to a low-order difference scheme near the boundary (LEVEQUE 2002). Incidentally, the above selection of the ghost cells also results in placing the reflecting boundary on the cell interfaces. It will be shown by comparison of MOST and Cliffs results that the positioning of the reflecting boundary within a cell (with or without ghost cells) could make significant difference specifically for splitting schemes, when a 2D problem is approached as a sequence of 1D problems.

Both MOST and Cliffs reflection algorithms demonstrated highly accurate and visually identical results while computing wave reflection on a boundary oriented strictly along the x or y axis (after correction for a half-cell difference in positioning of the reflecting wall). The difference in solution appears when a reflecting boundary is oriented at an angle to the coordinate axes. This difference is due to 1D nature of the splitted computations. Unless a straight boundary coincides with either x or y axis, it can not be treated by a splitted scheme as straight, but rather as a step-like. Consider, for example, a diagonal channel shown in Fig. 2, left. When the MOST solver performs computations in x direction, it “sees” this boundary as a set of steps whose vertical segments are aligned with the edge wet nodes, as shown on the north-west channel boundary with a black line (Fig. 2, left). When computations are performed in y direction, the solver “sees” a different set of steps. Now the horizontal segments of the steps are aligned with the edge nodes, as shown by a gray line on the north-west boundary. Cliffs “sees” the same step-like boundary for both directions of computations, which is located in-between wet and dry nodes as shown on

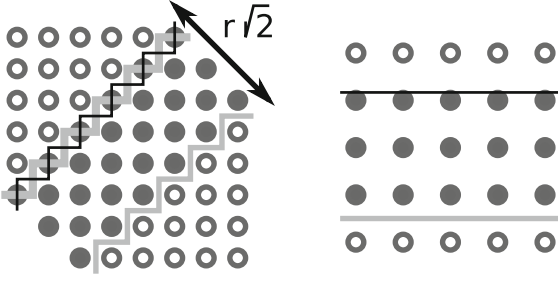


Figure 2

Black dots water, circles land. *Left* diagonal channel at Δx spacing, water in nodes (i, j) such that $|i - j| < r$, $r = 3$. Land-water boundary seen by MOST in x direction (black line) and in y direction (gray line) are shown on north-west channel boundary. Land-water boundary seen by Cliffs in either direction is shown on south-east channel boundary. *Right* a channel at $\sqrt{2}\Delta x$ spacing oriented along x axis. Land-water boundary seen by MOST (black) is shown on the north. Land-water boundary seen by Cliffs (gray) is shown on the south

the south-east channel boundary. As the next simulation shows, the roughness of the reflecting boundary and especially its displacement due to different alignments for different directions of computations results in dissipation of the reflected wave. This effect is more significant for shorter waves.

4.1. Simulation of N-wave in a Channel

Let us compare MOST and Cliffs solutions for a plane N-shaped wave propagating in a straight channel between two reflecting walls, for two computational set-ups. In the first set-up, the channel was oriented along x axis (Fig. 2, right). Computational domain was represented by (11×401) -node grid at $\Delta x = \sqrt{2}$ m spacing, with rows 2 to 9 being water $d = 1$ m deep, and the first and last rows being high elevated land. N-shaped initial surface deformation centered on 201-th node, function of x coordinate, was given by

$$\eta_0(x) = 2a \cosh^{-2} \left(\frac{x - x_{201}}{\sqrt{2}w} \right) \tanh \left(\frac{x - x_{201}}{\sqrt{2}w} \right), \quad (15)$$

with parameters a and w being used to manipulate the pulse amplitude and width.

In the second set-up, the channels of different width were oriented along the main diagonal of a (401×401) -node grid at 1 m spacing. Nodes

(i, j) , $i, j = 1, \dots, 401$ with such numbers that $|i - j| < r$ were in water 1 m deep, and the other nodes were land, which corresponds to $r\sqrt{2}$ m distance between rows of dry nodes on the sides of the channel (Fig. 2, left). According to the implied position of the reflecting walls, the channel width for Cliffs is $0.5\sqrt{2}d$ less, and for MOST, it is $\sqrt{2}d$ less than the distance between the dry rows. Initial surface deformation centered in node $(201, 201)$, function of x, y coordinates, was given by

$$\tilde{\eta}_0(x, y) = 2a \cosh^{-2} \left(\frac{(x - x_{201}) + (y - y_{201})}{2w} \right) \tanh \left(\frac{(x - x_{201}) + (y - y_{201})}{2w} \right) \quad (16)$$

Initial deformations (15) and (16) are identical, both in continuous and discrete form, when viewed along the centerline of the corresponding channel.

Time increments Δt for the computations were 0.42 s with the first set-up, and 0.3 s with the second set-up, which provides nearly the same ratio $\sqrt{gd} \cdot \Delta t / \Delta x = 0.93, 0.94$ in the two cases. At this value of the Courant number, numerical dispersion and dissipation inherent to the MOST model are negligible (BURWELL *et al.* 2007). Thus the expected solution would be an N-wave with the leading peak propagating from the center of the channel to the right, and an identical N-wave with the leading trough propagating from the center of the channel to the left, without change in shape. Factor a was selected to normalize each N-wave peak amplitude to 1 cm.

In the first set-up, both MOST and Cliffs provided visually identical solutions, close to the expected solution which does not depend on the width of the channel. In the second set-up, MOST and Cliffs solutions differ from each other and from the solution in the x axis-channel.

Instant surface profiles along the centerline of the diagonal channels of three different widths computed with the two models, and the x axis-channel solution are shown in Figs. 3 and 4. The profiles are taken at $t = 67.2$ s, or after each N-wave traveled $212d$. In Fig. 3, the initial N-wave with $w = 10$ was $14\sqrt{2} \approx 19.8d$ wide between the trough and the peak. The distance between the diagonal rows of dry nodes on the channel sides, from wide to narrow (top to bottom in the figures), was approximately $26.9d$ ($r = 19$),

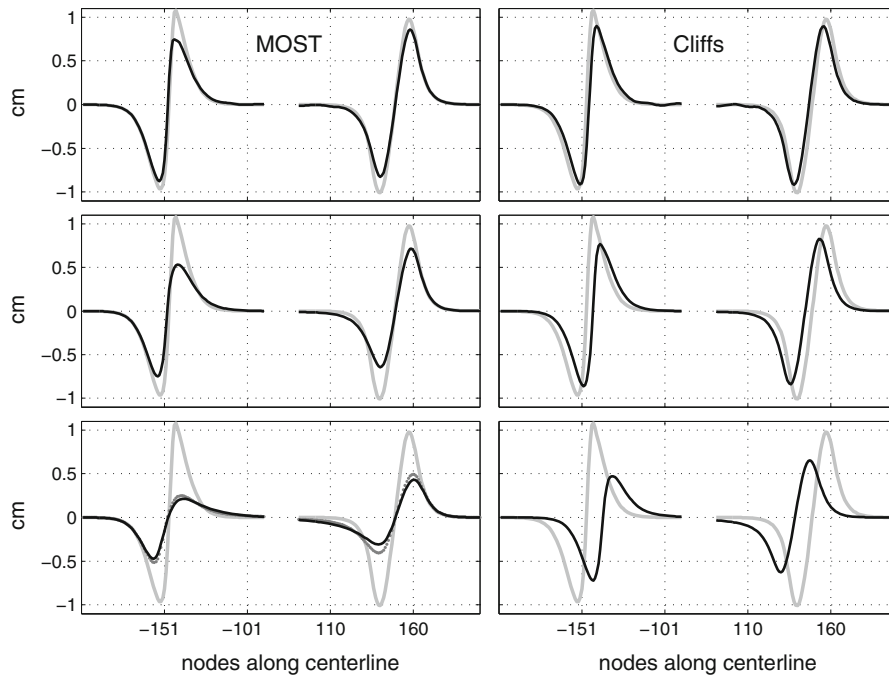


Figure 3

Surface profiles of longer N-waves ($w = 10$) along a channel centerline at $t = 67.2$ s in a channel oriented along x axis (gray), and in a channel oriented diagonally (black solid) computed with MOST (left panes) and Cliffs (right panes) with the same computational grid. MOST solution computed on a grid with an extra row of wet nodes (to match the actual width of wet area with Cliffs) is shown in the narrowest channel only (gray dots). Top to bottom channel width $26.9d$, $12.7d$, and $5.7d$. Spacing between nodes on the centerline $\sqrt{2}d$, $d = 1$ m

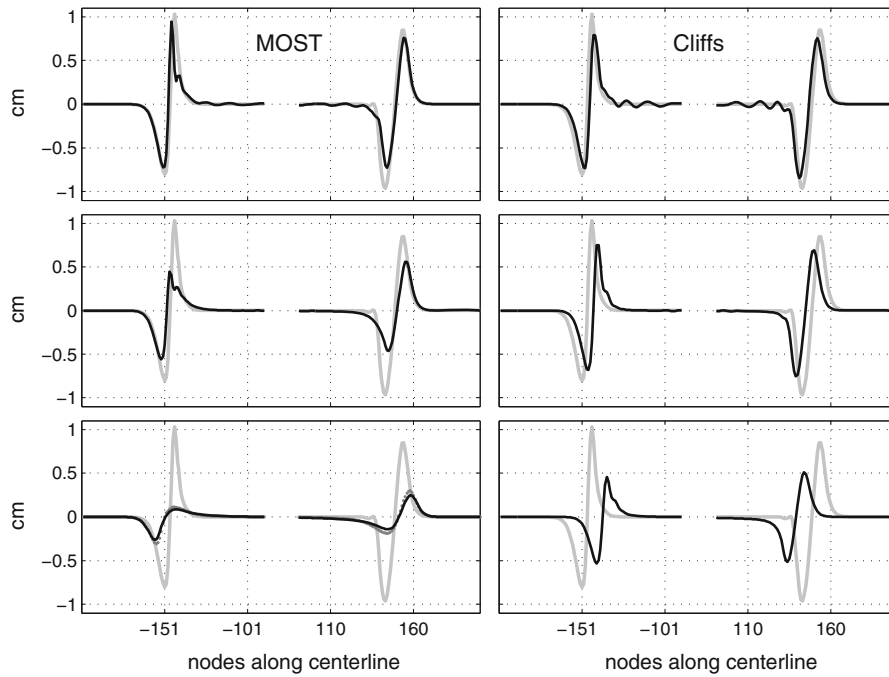


Figure 4

Surface profiles of shorter N-waves ($w = 5$) in the diagonal channel, in the same configurations as in Fig. 3 above

$12.7d$ ($r = 9$), and $5.7d$ ($r = 4$). Two MOST solutions were computed per each Cliffs solution. The first MOST solution uses the same grid with the Cliffs solution, which corresponds to a channel $0.5\sqrt{2}d$ narrower for MOST. The second MOST solution uses a grid with an extra diagonal row of wet nodes, which corresponds to the same channel width with Cliffs. The difference between the two MOST solutions is visible only for the narrowest channel.

All MOST and Cliffs solutions are lower in amplitude the narrower the channel, compared to the x axis-channel solution. Both MOST solutions in each case are more diffused than the corresponding Cliffs solution. The MOST solution is also more asymmetric with respect to N-waves with leading peak and with leading trough. This tendency is more easily seen in Fig. 4 showing profiles of the half as short N-wave with $w = 5$.

A particular feature of the Cliffs solution in a diagonal channel is that it is delayed in time. Given that the channel walls are step-like rather than smooth (as shown in Fig. 2), the effect can possibly be explained by the mere friction exerted by the walls. The friction acceleration experienced by a water slice in the channel's cross-section is inversely proportional to the mass of the slice and thus to the channel width, hence the effect is greater the narrower the channel. For MOST, the channel walls move within a time step, which apparently offsets the time delay and increases the dissipation. No time shift between Cliffs and MOST solutions has been observed in further simulations of real-world scenarios and lab experiments.

Overall, wave dissipation in a diagonal channel is greater the smaller the wavelength and the narrower the channel, and it is greater with MOST than with Cliffs.

4.2. Simulation of Tohoku-2011 Tsunami from the Source Earthquake to Monterey Bay

We have demonstrated that the two reflection algorithms can return noticeably different results in the specific settings (a long narrow diagonal channel). Now let us show that the results might be different for an ordinary, real-world settings as well.

In the NOAA's Center for Tsunami Research (NCTR), MOST is used with the solid-wall boundary conditions, in particular, for ocean-wide propagation database computations. The propagation database is then used to provide boundary input into higher resolution inundation models at selected locations (TANG *et al.* 2009). The March 11, 2011 Tohoku tsunami was simulated Pacific-wide with MOST and Cliffs. The tsunami source is the one used in NCTR (TANG *et al.* 2012). A computational grid developed from the ETOPO-1 dataset, NGDC extends from 100°E to 60°W , and from 75°S to 64°N . As adapted for ocean-wide computations in the NCTR, simulations were carried at a 4 arc-min (7 km near the equator) resolution in longitude and latitude. To exclude any run-up/run-down calculations, a reflecting wall was introduced at 20 m depth. Figure 5 shows the simulated tsunami time histories at two deep-ocean locations offshore Japan. Being virtually

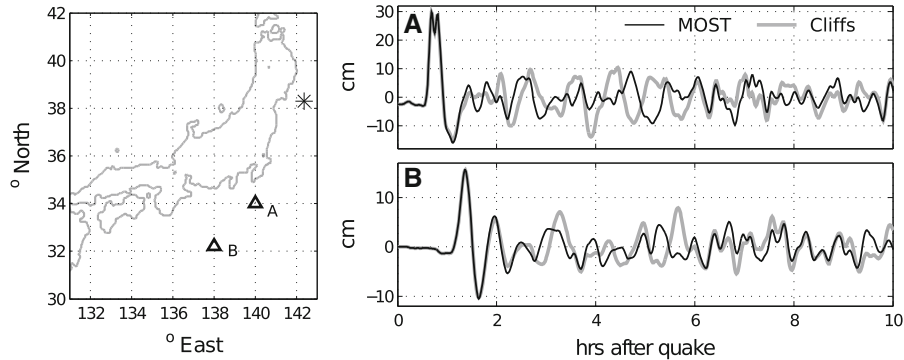


Figure 5

Left star epicenter of the Tohoku-2011 earthquake, triangles observation points A and B. Right Tsunami time histories at the observation points simulated with MOST (black) and Cliffs (gray)

identical for the direct wave train, the MOST and Cliffs solutions are apparently different in the later waves reflected by the complex coastline.

It's been shown that later in a tsunami event, the tsunami energy in the Pacific ocean decays exponentially, with the e-folding time being approximately 22 h (VAN DORN 1984). TANG *et al.* (2012) estimated the e-folding decay time of the Tohoku-2011 tsunami simulated with the latest MOST version (which is the version used in this work) to be only 17.6 h, even though the use of the vertical wall in 20 m deep water might suggest less dissipation for the reflected waves than would occur in nature. A possible reason for the opposite is that the roughness of the numerical shorelines was increased by the step-wise approximation with a 7-km-wide step, while in the real world, the roughness is distributed among the continuum of space scales, with the smaller features causing less wave diffusion. Figure 6 shows decay of the Tohoku-2011 tsunami in the Pacific simulated with MOST and with Cliffs, vs. the decay path corresponding to the 22 h e-folding time. As seen in the plot, Cliffs preserves the energy of the reflected waves better than MOST does. After 24 h of the

elapsed time, the wave energy in the Cliffs solution domain-wide contains 113 % of the wave energy in the MOST solution.

Next, the ocean-wide solution was refined with two nested regional grids narrowing on Monterey bay, CA. The outer grid at a resolution of 45 arc-sec of the Great arc covered the Northern California coast, while the inner grid at 8 arc-sec resolution enclosed the bay and its surroundings. Reflective boundary conditions were imposed at depth 1 m. Figure 7 shows the Tohoku-2011 tsunami time histories, recorded at the tide gage and simulated with either MOST or Cliffs. A simulation performed with MOST from the source earthquake matched the record's envelope well (subject to limited knowledge about the tsunami source function) for about 3 h, until a 13 h mark. A simulation performed with Cliffs from the source earthquake matched the record for twice as long, until a 16 h mark. The better results by Cliffs is due to better representation of later waves reflected from the coasts in the ocean-wide simulation. Very little difference in the results by MOST and Cliffs in Monterey Bay is observed, should the regional simulations use the same boundary input from the Pacific-wide simulation.

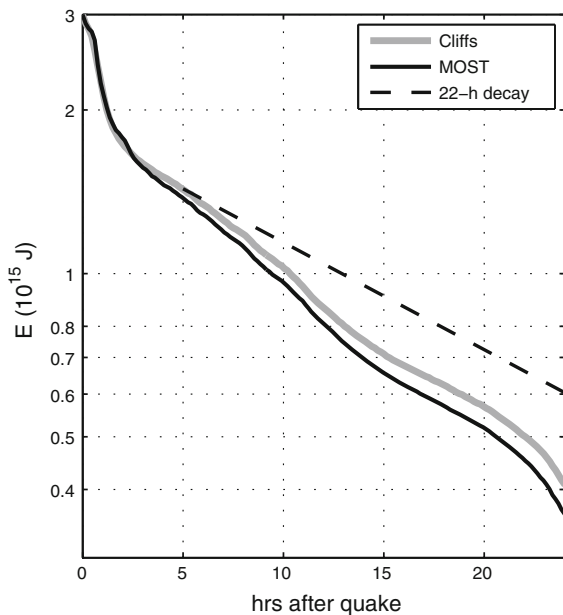


Figure 6

Time histories of the domain-integrated energy of the Tohoku-2011 tsunami in the Pacific simulated with MOST and with Cliffs.

Dashed line shows the decay with the 22 h e-folding time

4.3. Simulation of Tohoku-2011 Tsunami in Southeast Alaska

The difference in regional simulations by MOST and Cliffs is expected in a fjord-like environment, even under the same boundary input from the Pacific. Examples of such environments are the entire Pacific side of Canada and southeast Alaska, United States, their continental coasts and the shores of nearby islands. Next, the 2011 Tohoku tsunami is simulated with MOST and Cliffs in southeast Alaska. The simulation results are compared location-wise between the two models and with local tide gage records.

Two levels of bathymetric/topographic regional grids were used to model the tsunami propagation in southeast Alaska. The regional grids were derived at 60 s of Great arc (outer grid) and 16 s of Great arc (inner grid) resolution, using bathymetric and topographic data from the National Geophysical Data Center ETOPO1 database and Southern Alaska 8 s DEM. The grids extent is shown in Fig. 8, left panel.

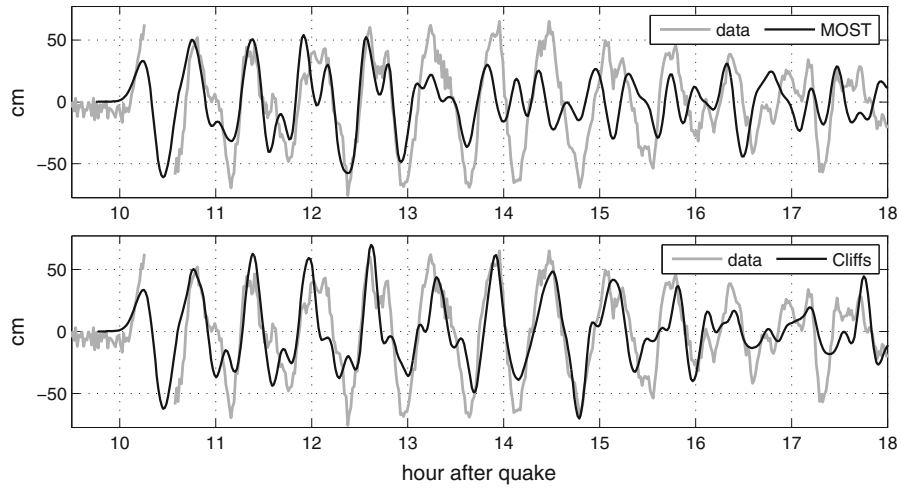


Figure 7

Top Tohoku-2011 tsunami at Monterey Bay tide gage, recorded (gray) and modeled with MOST (black); bottom the same, modeled with Cliffs. All simulations are delayed 8 min

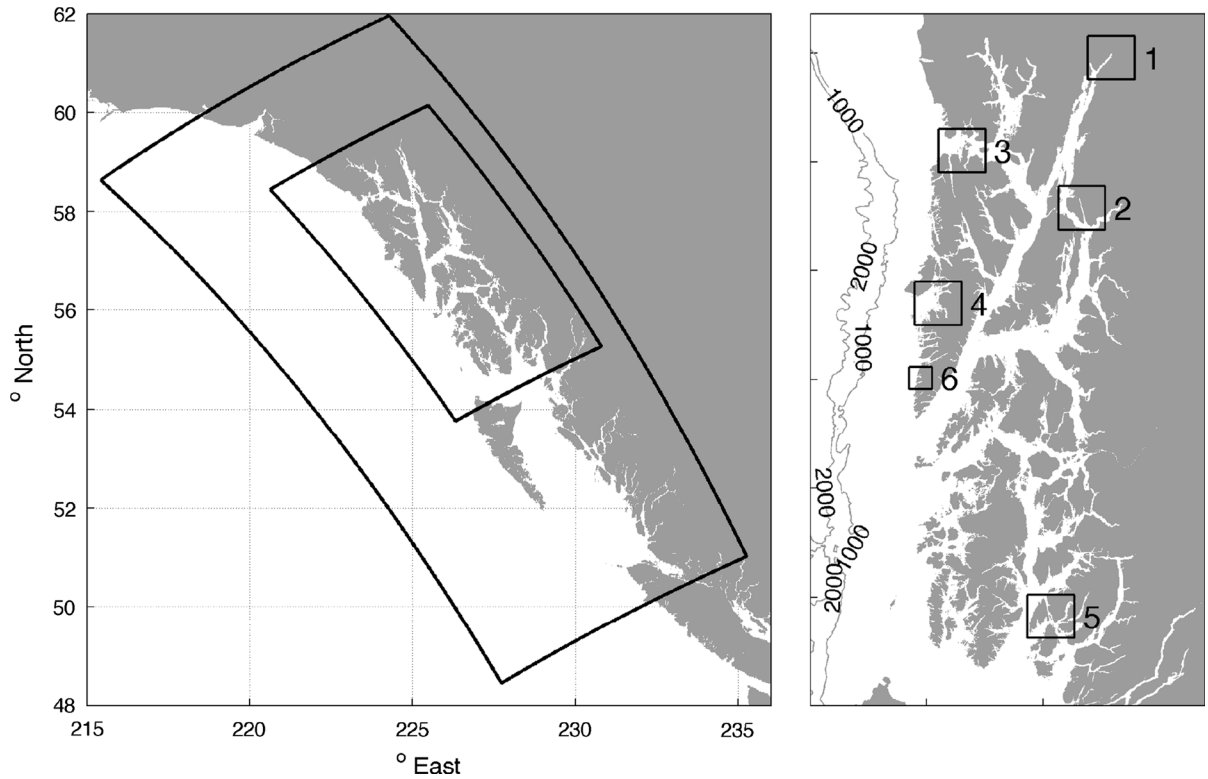


Figure 8

Left extent of two nested regional level grids for the Tohoku tsunami simulations in Southeast Alaska (the grids are developed in a spherical coordinate system whose equator is aligned with the shoreline). Right the inner regional grid; boxes denote areas around actual or virtual gages zoomed-in in Fig. 9; 1 Skagway, 2 Juneau, 3 Elfin Cove, 4 Sitka, 5 Ketchikan, 6 unnamed bay; depth isolines are drawn at 1,000 and 2,000 m

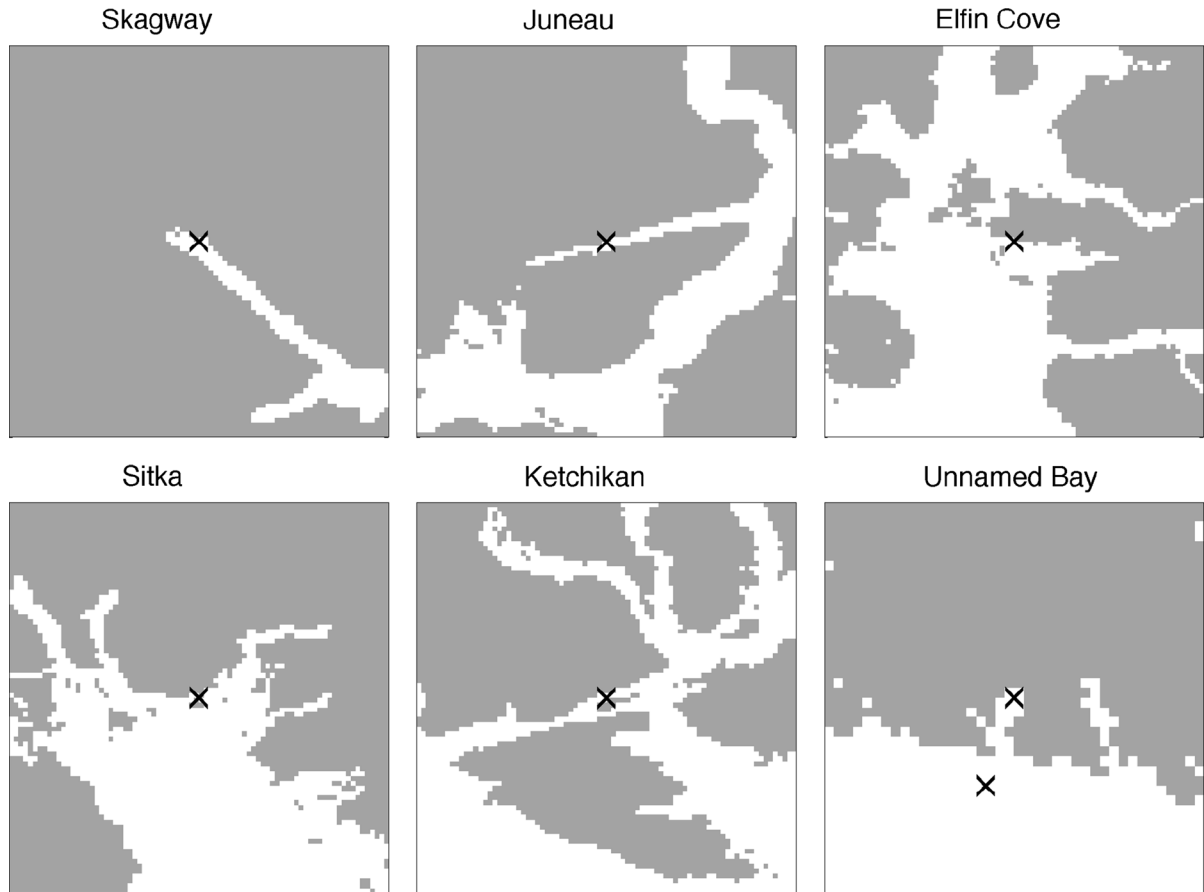


Figure 9

40 × 40 km areas around tide gages in Skagway, Juneau, Elfin Cove, Sitka, and Ketchikan; 20 × 20 km area enclosing unnamed bay, at 16 arc-sec (0.5 km) space resolution; *crosses* mark locations of actual or virtual gages. For locations of displayed areas on a larger map see Fig. 8, right panel

Computations at the regional level were performed with MOST and with Cliffs, under the same boundary input from the Pacific-wide simulation of the tsunami (8 min delay is applied to the boundary input) computed with Cliffs as above. The Tohoku tsunami has been recorded at six tsunami-capable (sampling at 1 min interval) NOS gages throughout the area, namely in Skagway, Juneau, Elfin Cove, Sitka, Ketchikan, and Port Alexander. Location of the gages is shown in Fig. 8, right panel, and zoomed-in in Fig. 9. According to gage records (Fig. 10), wave motion at Skagway, Juneau, and Ketchikan, separated from the open ocean by multiple topographic features, is dominated by components with periods longer than 20 min, which in depth 50 m corresponds to wavelengths longer than 28 km. There is some presence of shorter-period waves at Sitka and Elfin

Cove, which face the ocean more directly. Given the inner regional grid resolution 0.5 km, we expect to capture the major part of tsunami signal at all locations except Port Alexander where the record is heavily dominated by an oscillation with 9 min period. Since the recorded tsunami amplitude was well under 1 m at any gage, little of runup/rundown action could take place, which, together with a relatively coarse resolution, justifies for using reflective boundary conditions on the shoreline.

Simulated time histories at the gages computed with MOST (left) and Cliffs (right), and the de-tided gage records are shown in Fig. 10 (comparison at Port Alexander is omitted). The solutions by MOST and Cliffs display fairly minor differences in Skagway, Sitka, and Elfin Cove. However, there are significant differences between the models at

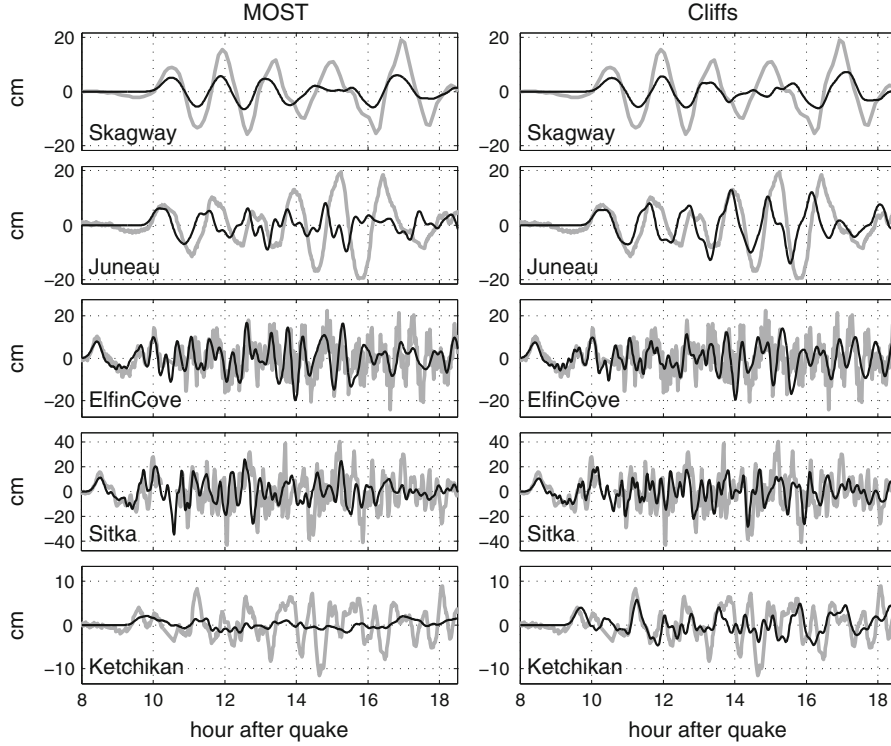


Figure 10

Simulated (*black*) and recorded (*gray thick*), tide removed, tsunami time-histories at NOS tide gages; *left* computations with MOST, *right* computations with Cliffs. All simulated time histories are delayed 8 min

Ketchikan and Juneau gages located in narrow channels (see Fig. 9). Cliffs solution matched the gage records as well as in other locations, subject to the accuracy of the tsunami source estimate. MOST clearly was not able to propagate the wave through the narrow channels without loss of the signal.

A sample location where the two models provided very different solutions is an unnamed bay in the mouth of Maksoutof river on the west side of the southern tip of Baranof Island. The bay is about 20 m deep and 4 km long, which results in a natural period of about 18 min. MOST and Cliffs solutions at a location inside the bay and a location outside the bay near its entrance (see Fig. 9 for the locations) are shown in Fig. 11. As seen in the top panel of the figure, the solutions by the two models outside the bay are close. The tsunami approaching the bay displays strong presence of motion at 18–19 min period. In the Cliffs solution, the bay's resonance is exited, while in the MOST solution, numerical damping on the shoreline completely stopped the resonance from developing (Fig. 11, lower panel).

As seen from the above simulations, to correctly reproduce even long (well-resolved) waves domain-wide with MOST, all sub-basins responding in tsunami frequency range should be over-resolved, whereas Cliffs is less subjected to this limitation.

5. From Vertical Wall to Sloping Beach

The use of the dimensional splitting implies that faces of the topographic features are always normal to the direction of computations, which is possible only when the topography is represented by cell-centered step-wise functions. The latter defines a moving shoreline as a set of cell interfaces separating cells which are wet or allowed to get wet from cells which are dry and expected to stay dry through the next time step. If the fluxes are given on cell interfaces, the change in the water volume in each cell, and therefore wetting and drying of a cell, is entirely determined by the fluxes into that cell. The latter readily translates into a runup algorithm suggested in

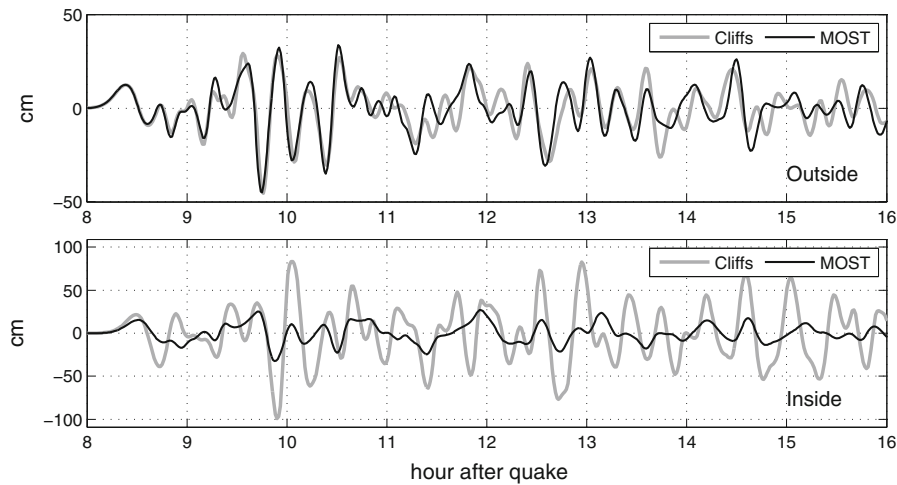


Figure 11

Tsunami time-histories at a virtual gage outside of unnamed bay (*top*), and inside the bay (*bottom*), computed with MOST and Cliffs

LIU *et al.* (1995) for a model later known as COMCOT (the Cornell Multi-grid Coupled Tsunami model). Similar wetting-drying schemes are often preferred by the newer models (NICOLSKY *et al.* 2011; IIMAMURA 2009). COMCOT explicitly sets fluxes on the shoreline to zero, while Alaska Tsunami Model (NICOLSKY *et al.* 2011) introduces penalty terms to impose no flow into the dry domain. An inundation algorithm of this kind applies reflective boundary conditions on a moving shoreline, and therefore incorporates reflection as a limiting case.

However, reflective boundary conditions adapted in VTCS-2 and in the present MOST model cannot be applied on a moving shoreline, because these conditions rely on the assumed direction of characteristics. TITOV and SYNOLAKIS (1995,1998) specifically noted that “it is impossible to use the direct relationship between the Riemann invariants... near the shoreline”, because of a possibility that “both characteristic families have the same inclination in this region”. Instead, an empirical 1D inundation algorithm had been suggested which introduces a temporal grid node at an instant shoreline defined by a horizontal projection of the water surface in the last wet node (TITOV and SYNOLAKIS 1995,1998) onto the linearly interpolated topography. It was not specified how to apply this algorithm in a situation when the projection does not meet land. This situation arises, for example, when modeling a canonical runup on a

conical island (see Sect. 6.2). Figure 17, right, shows wet/dry cells in a cross-section on the lee side of the island perpendicular to the direction of the wave attack, at some moment when runup on the lee side is in progress. The land profile is an arc with the running-up water being on the top of the arc. The horizontal projection of the water surface cannot yield an instant shoreline position in this direction of computations. Some modifications to the VTCS-2 runup algorithm had enabled the MOST model to handle various real-world topography. However, the details of the MOST runup computations have not been released, which is yet another incentive to develop an alternative runup algorithm to use with the VTCS-2 propagation scheme.

At the same time, Cliffs boundary conditions use no assumptions about the direction of the characteristics, which makes it possible to apply them on a shoreline as well. Thus wave propagation over dry land can be computed by combining the moving boundary treatment similar to that of the COMCOT model, with the boundary conditions (13)–(14). Further details of the runup algorithm are implied by specifics of the MOST formulation.

In particular, a feature of the MOST model is that its formulation does not allow a wet node to turn dry, because the equation (10) for the water depth is unlikely to return exact zero. To claim the land on rundown, a common procedure of comparing the

water depth with an empirical threshold h_{\min} is used. When the depth is less than the threshold, the cell is marked as dry. For the inundation algorithm been developed, it means that when a dry cell is to be flooded and thus added to a wet segment, it has to be pre-filled with water to h_{\min} depth. One cycle of the resulting solution procedure in a basin with arbitrary topography follows:

- The water height in each cell is compared with a threshold h_{\min} . When the height is less than the threshold, the cell is marked as dry.
- For each neighboring i -th dry and j -th wet cells ($j - i = \pm 1$), a decision is made on including the dry cell with the wet segment. Namely, **if** the particle velocity u_j in the wet cell is directed shoreward **and** the flooding depth is greater than h_{\min} , that is, $h_j - d_j + d_i > h_{\min}$, **then** i -th cell becomes wet with water column height h_{\min} and velocities equal to those in the adjacent wet cell (Fig. 12, left).
- Once the wet/dry segments are finalized, conditions (13)–(14) are applied on the wet/dry interfaces.
- In all wet nodes, the solution for the next time step is computed according to (7).
- The updated water height h_i in each newly added wet cell on the shoreline is compared with the water height in the neighboring wet cell h_j .

Should the computation result in $h_i > h_j/2$, then the water height and velocities in i -th cell are replaced with $h_j/2, u_j/2, v_j/2$ respectively. This operation ensures that linearly extrapolated water surface and land surface intersect landward from node i at a distance not greater than the distance between the i -th and j -th nodes (Fig. 12, right).

Using reflecting boundary conditions throughout yields an analogy of framing wet segments with moving mirrors (cliffs). The run-up and run-down are made possible by expanding the wet area in step (b) and shrinking it in step (a). Since the solver (7) uses a centered 3-node pattern, the wave can propagate only as far as one cell per a time step, thus the wet area is also expanded by no more than one cell on each side. The runup occurs on an inserted cushion h_{\min} high, which is removed on rundown.

A distinct feature of the Cliffs algorithm is the active role played by the runoff cushion. In addition to helping to maintain mass conservation, the runoff cushion adds landward directed flux, which tends to compensate for the momentum loss through vertical faces of the stairs representing a beach. The loss of momentum occurs via landward flux to a ghost cell and an equal opposite flux from the ghost cell while a wet cell on the shoreline is being filled from height h_{\min} to $h_{\min} + d_j - d_i$. However, once the wet cell can inundate, landward flux $u \cdot h_{\min}$ is added with the

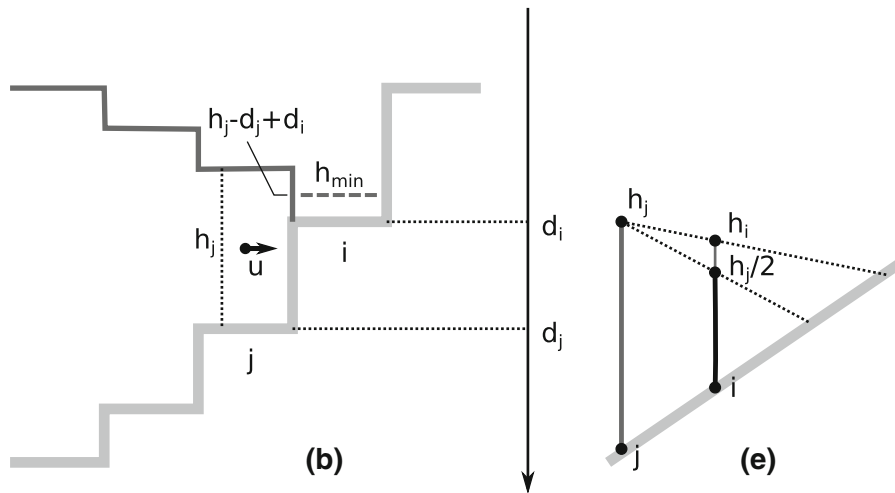


Figure 12

Illustration to step **b** i -th dry cell will be filled to h_{\min} level and included with the wet segment; step **e** should the computation result in $h_i > h_j/2$, then the water height and velocities in the newly included i -th cell are set to half these in the j -th cell

cushion in step (b). Hence increasing the threshold increases the runup (for small h_{\min}). It will be demonstrated in Sect. 6.1 that the optimal threshold is a half to a whole land elevation increment $d_j - d_i$. At these values of h_{\min} , the runup reaches as far as the wave would propagate onto a smooth plane beach. Increasing the threshold further results in more frequent corrections to the solution in step (e) which has the effect of thinning the cushion and consequently reducing the runup. As the result, the computed runup only mildly depends on the choice of h_{\min} in a broad range of threshold values. The threshold also limits the height of the wave permitted to inundate.

Cliffs inundation algorithm is about 10 % more efficient in terms of computational time than the present MOST algorithm.

6. Testing Cliffs Inundation Algorithm

In this section, Cliffs is tested with some benchmark problems adapted by National Tsunami Hazard Mitigation Program (NTHMP) following NOAA's standards and criteria (SYNOLAKIS *et al.* 2007; NTHMP 2012), with an emphasis on testing the inundation algorithm. Cliffs solutions to the benchmark problems are compared to the MOST solutions obtained with the version of the MOST model benchmarked for NTHMP in 2011. Given that MOST and Cliffs share the same propagation part, this comparative benchmarking provided a rare opportunity to observe variability in the results due specifically to an inundation algorithm. Whenever the solutions by the two models are different, both solutions are shown. Detailed descriptions of all benchmarks, as well as topography and laboratory or survey data when applicable, can be found in a repository of benchmark problems <https://github.com/rjleveque/nthmp-benchmark-problems> for NTHMP, or in the NCTR repository <http://nctr.pmel.noaa.gov/benchmark/>.

6.1. Single Wave on Simple Beach

SYNOLAKIS (1987) performed a set of laboratory experiments to investigate run-up of breaking and non-breaking solitary waves of initial height H over

depth d normally incident onto a plane sloping beach, and suggested an analytical treatment for the run-up of the non-breaking waves. These experimental and analytical results have become a canonical case for validation of runup models.

The geometry of the beach, the lab experiment, and the wave-profile are described in many articles (SYNOLAKIS 1987; TITOV and SYNOLAKIS 1995; SYNOLAKIS *et al.* 2007) as well as in the Internet repositories mentioned above. The 1D bathymetry consists of a flat segment of depth d connected to a beach with a slope 1:19.85. The x coordinate increases seaward, $x = 0$ is the initial shoreline position, and the toe of the beach is located at $x = 19.85d$. With the height, width, and distance of the initial wave-surface profile from the toe of the beach being proportional to d , it is common practice to express the results in dimensionless units of length and time.

The cases with $H/d = 0.0185$ and $H/d = 0.3$, representing a non-breaking and a severely breaking wave respectively, are most commonly used for model verification (LI and RAICHLEN 2002; WEI *et al.* 2006; ROEBER *et al.* 2010; NICOLSKY *et al.* 2011) against laboratory and analytical data of Synolakis. These two cases are simulated below.

The simulation of a solitary wave runup in this work was performed with a 384-node grid, which encompassed a $45d$ -long segment of constant depth d connected to $50d$ -long 1:19.85 slope. In simulations, the depth of the flat part of the basin was $d = 1$ m. The grid spacing was set to 1 m (depth) over the flat segment, and then varied as \sqrt{d} , but not less than $0.1d$. Time increment $\Delta t = 0.03$ s yields Courant number $\Delta t \sqrt{gd}/\Delta x = 0.1$, thus providing for emulating physical dispersion with numerical dispersion (BURWELL *et al.* 2007; TOLKOVA 2012). Friction coefficient was set to zero. Depth threshold h_{\min} was set to 3 mm. Results with dimension of length are expressed in units of d , time is expressed in units of $\tau = \sqrt{d/g}$.

Like many other tsunami models (NTHMP 2012), Cliffs had no difficulty in closely reproducing the analytical solution and the laboratory measurements in the case of a low-amplitude non-breaking wave. Figure 13 shows water surface profiles computed with Cliffs for the non-breaking wave vs. lab measurements and analytical solution according to

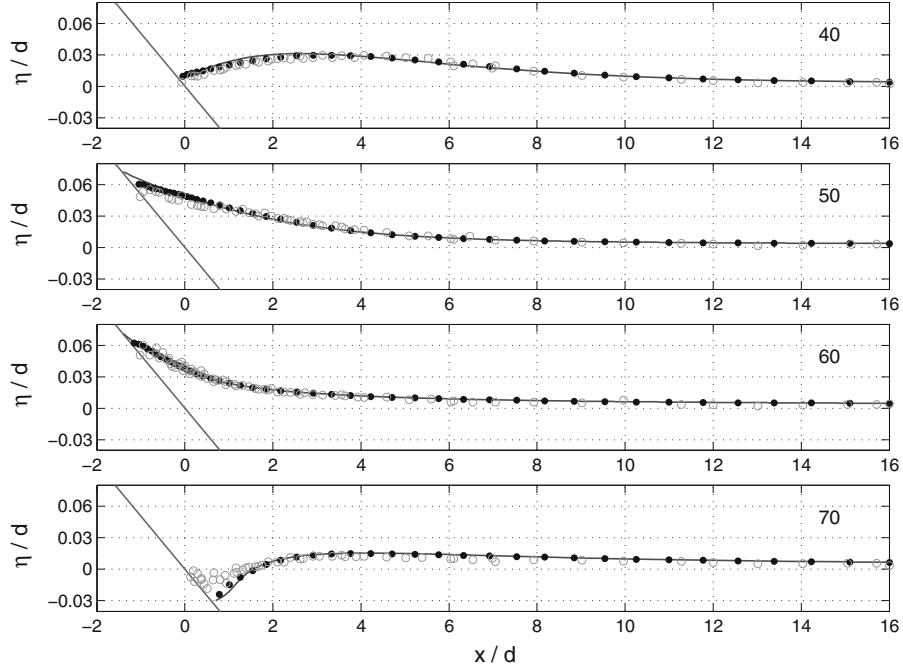


Figure 13

Water surface profiles for an initial solitary wave $0.0185d$ high climbing up a $1:19.85$ beach at $t(g/d)^{1/2} = 40, 50, 60, 70$ (shown in a plot), gray circles measurements, black dots Cliffs numerical solution, black line analytical solution

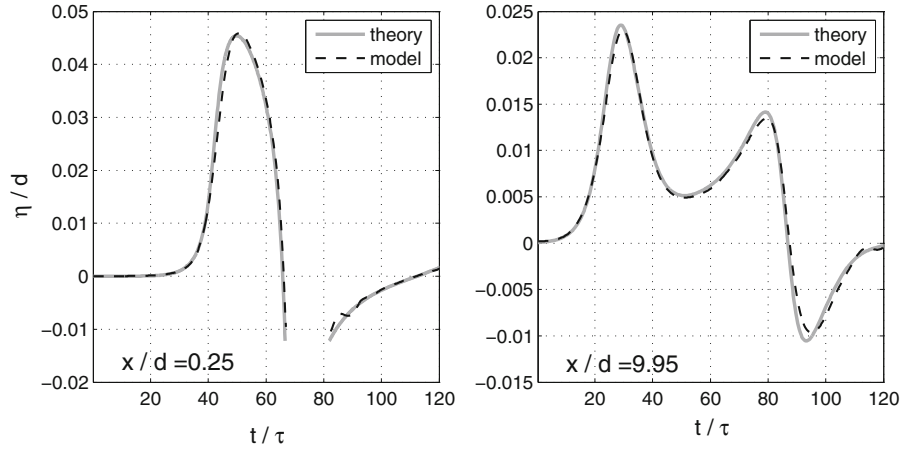


Figure 14

Water surface time histories at locations $x = 0.25d$ ($0.014d$ deep) and $x = 9.75d$ ($0.517d$ deep) in a solitary wave of $0.0185d$ initial height: Cliffs numerical solution (black dashed) vs analytical solution (gray). The solutions are interrupted in the first location, when the location temporally dries out

SYNOLAKIS (1987). Figure 14 shows surface elevation time histories computed with Cliffs for the non-breaking wave vs. the analytical solution. Cliffs solution for this case is very close to the MOST solution (not shown).

Modeling the case of a breaking wave presents a number of challenges, though more advance models do fit the measurements very closely (ROEBER *et al.* 2010). Non-dispersive models commonly develop a vertical leading front shortly after the beginning of

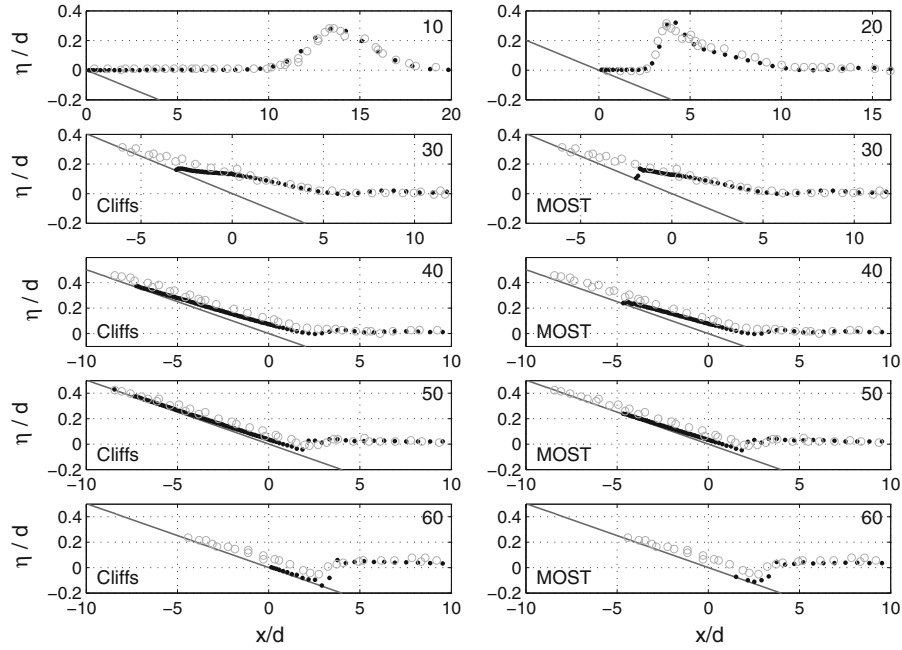


Figure 15

Water surface profiles for an initial solitary wave $0.3d$ high climbing up a $1:19.85$ beach at $t/\tau = 10, 20, 30, 40, 50, 60$ (as written in a plot), gray circles measurements, black dots - numerical solution by Cliffs and MOST. MOST solution, when different, is shown on the right of the corresponding Cliffs solution

computations (NICOLSKY *et al.* 2011). The numerical singularity propagates to the shoreline and becomes a thin layer of liquid climbing up the slope. By making use of the numerical dispersion inherent to the MOST difference scheme, we avoid developing the singularity and fit the measurements almost all the way up to the shore, as seen in Fig. 15. The disappearance of the discontinuity in the Cliffs solution occurs at $t/\tau = 25+$, shortly after the actual wave broke (between 20 and 25 τ). Consequently, the Cliffs run-up is slightly delayed in time, but eventually reaches as far as the actual wave did.

In this case, MOST and Cliffs solutions are identical until the wave touched the original shoreline at 25τ . From that moment, the shoreline in the MOST solution travels behind both the measurements and the shoreline in the Cliffs solution, as seen in Fig. 15. MOST runup reaches only $0.275d$ high, whereas the measured runup height, also computed by Cliffs, is $0.431d$.

Figure 16 shows maximum runup and rundown computed by Cliffs with different values h_{\min} varying from 0.5 mm to 2 cm. The same values were also

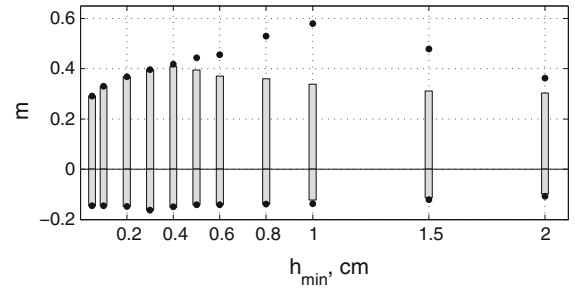


Figure 16

Maximum runup and rundown elevation (gray bars) in a solitary wave $0.3d$ high, $d = 1$ m, propagating onto a $1:19.85$ beach, computed with Cliffs at different values h_{\min} . Black dots denote maximum runup and rundown computed by Cliffs inundation algorithm with omitted step (e). Difference in land elevation in neighboring dry cells is 0.5 cm

computed with step (e) omitted. To keep the solution stable at marginally small thresholds (1 mm or less), very little friction with $n = 0.005$ was included. Given $d = 1$ m and the grid spacing on land $0.1d$, the change in land elevation between beach nodes is 5 mm, which points to an optimal threshold range 3–5 mm. Outside this range, the runup is lower, whereas without step (e) it continues to grow with the

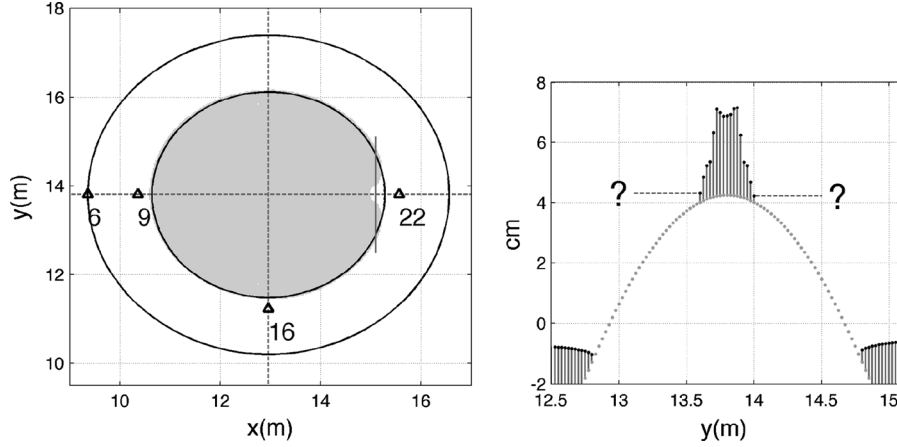


Figure 17

Left location of the gages around the island, island base on the basin floor, and the original shoreline as seen from the above. Wave comes from the left along the x axis. Gray color denotes dry area at 35.18 s in case B, when runup on the lee side is in progress. Right cells snapshot at $t = 35.18$ s in case B, in a section shown in the left plot by a vertical line at $x = 15.1$ m; black dots water surface elevation in wet cells, gray dots land elevation cell-wise. The horizontal projection of the water column next to the land (dashed lines in the right plot) cannot yield an instant shoreline position required for the VTCS-2 runup computations

threshold. As seen in the figure, dependance of Cliffs runup computations on the threshold is fairly mild, which is maintained in step (e). Perspectives of using a variable threshold over irregular topography has not yet been investigated.

6.2. Runup on a Conical Island

Reproducing a wave-tank experiment where a plane solitary wave attacks and inundates a conically shaped island is another popular test for tsunami inundation models (BRIGGS *et al.* 1995; LIU *et al.* 1995). A model of the conical island with 1:4 slope and 7.2 m diameter at the base was constructed near the center of a flat 29.3×30 m basin filled with water $d = 32$ cm deep. In three separate experiments, three different incident solitary waves were generated: $0.05d$, $0.1d$, and $0.2d$ high, labeled cases A, B, and C correspondently. In each case, time histories at several locations around the island, and the angular distribution of runup were recorded. The problem was simulated using two nested grids. The outer grid enclosed the entire basin area starting at the wave-maker. Boundary input into the domain was provided according to the paddle trajectories. Time increment of 0.01 s with the depth-equal spacing provided for imitating physical dispersion as the pulse propagated from the wave-maker toward the island. Run-up onto

the island was simulated within finer 10 m x 10 m grid spaced at 2.5 cm; the roughness coefficient for the basin concrete was $n = 0.012$; $h_{\min} = 2$ mm.

Simulated time histories at four gages closest to the island (gage 6 at depth 31.7 cm, gage 9 at 8.2 cm, gage 16 at 7.9 cm, and gage 22 on the lee side at depth 8.3 cm, see Fig. 17, left panel) vs. laboratory measurements for the three cases are shown in Fig. 18. The results by MOST and Cliffs at the gages are visually identical. The computed boundaries of inundated area around the island in each of the three cases vs. measurements are shown in Fig. 19, left. All three cases have been reproduced fairly accurately. Slight difference in runup computations by MOST and Cliffs can be seen in angular distribution of maximal runup height around the island, pictured in Fig. 19, right. Note that given the grid spacing, difference in the maximal runup by MOST and Cliffs under 0.6 cm corresponds to difference in a single node which has been inundated or left dry.

6.3. Lab Experiment with a Scaled Model of Monai Valley

The 1993 Hokkaido tsunami (see the next section) caused extreme runup at the tip of a narrow gully at Monai, Okushiri island, Japan. This event was reproduced in a wave tank experiment described in

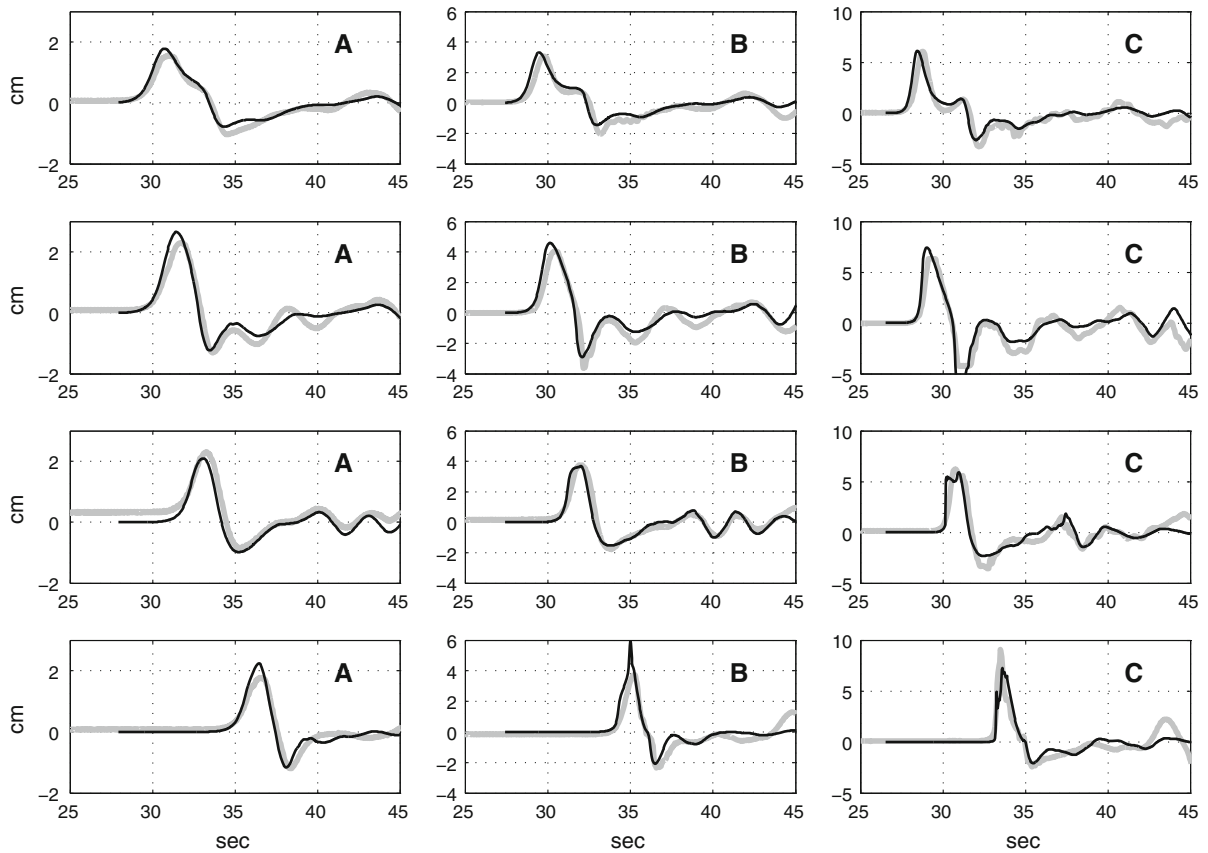


Figure 18

Time histories at the gages around the island, recorded (gray thick) and computed with Cliffs (black). Top to bottom gages 6, 9, 16, and 22; left to right cases A, B, and C

detail in LIU *et al.* (2008), SYNOLAKIS *et al.* (2007). The experiment focused on testing tsunami models for an ability to capture shoreline dynamics with an extreme runup and rundown over a complex topography, represents a 1:400 scale version of the tsunami event around Monai.

The domain of computations represents a 5.5×3.4 m portion of the tank next to the shoreline. Water level dynamics in this region were recorded on video and at three gages along the shoreline. Five frames extracted from the video record of the lab experiment with 0.5 sec interval (NICOLSKY *et al.* 2011) are shown in Fig. 20. The first frame occurred approximately at 15.3 s of the lab event time. The topography around the gully and the location of the gages are shown in the right bottom pane in Fig. 21.

The lab experiment has been modeled with a provided grid at 1.4 cm spacing, friction coefficient

$n = 0.012$, $h_{\min} = 1$ mm. The simulation reproduced the observations fairly well. Five snapshots of simulated water height distribution 0.5 s apart are shown in Fig. 21. The first snapshot was taken at 15.7 s. By visual comparison, the simulations agree closely with the recorded shoreline position in space and in time. Close fit is also observed between modeled and recorded water level time histories at the gages (see Fig. 22). Note that valid input into the model through the sea-side boundary of the domain was provided for the first 23 s only. Simulating this experiment with MOST yielded very close results (not shown).

6.4. Simulation of the 1993 Hokkaido–Nansei–Oki Tsunami

On July 12, 1993, the Mw 7.8 earthquake west of Okushiri island, Japan, generated a tsunami that has

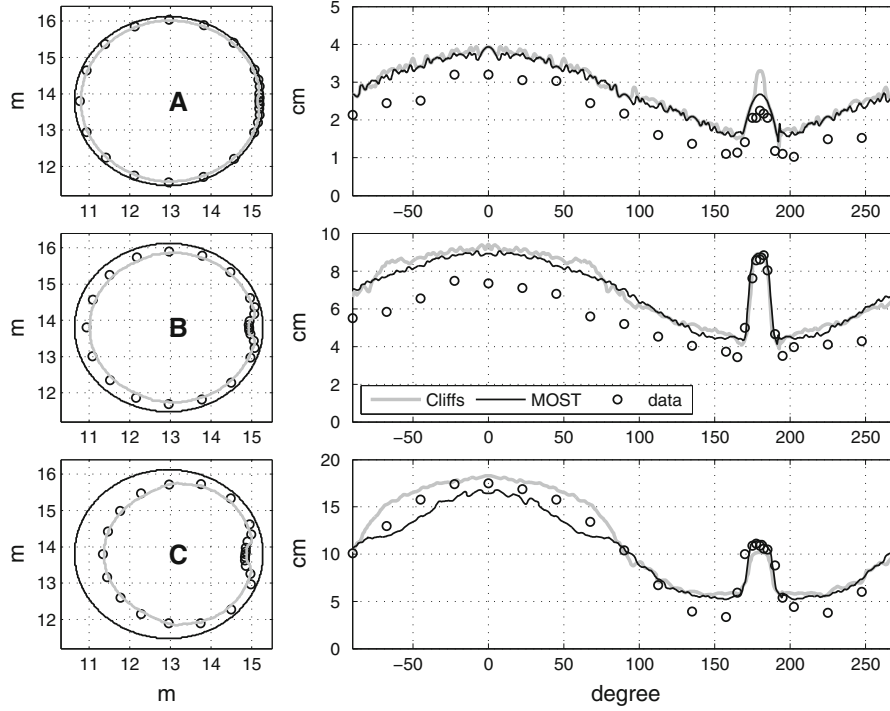


Figure 19

Left inundation line around the island: computed with Cliffs (gray), laboratory measurements (black circles), original coastline (black); wave attacks from the west. Right angular distribution of maximal runup height around the island, angle being counted counterclockwise from the west, computations with Cliffs and MOST, and the measurements. Top to bottom cases A, B, and C

become a test case for tsunami modeling efforts (TAKAHASHI 1996; SYNOLAKIS *et al.* 2007; NTHMP 2012). Detailed runup measurements around Okushiri island were conducted by the Hokkaido tsunami survey group which reported up to 31.7 m runup near Monai village. Also, high-resolution bathymetric surveys were performed before and after the quake, which allowed to evaluate the deformation of the ocean bottom due to the quake. The conventional practice in modeling geophysical tsunamis is to assume that the tsunami originates with the initial deformation of the sea surface following that of the ocean bottom.

Bathymetry/topography grids and the tectonic source information for simulating the Okushiri tsunami were originally developed for the 1995 Friday Harbor Long Wave Runup Model workshop (TAKAHASHI 1996). Those grids suffer from significant misalignments. As part of model benchmarking efforts by the NTHMP, a refined set of grids has been developed. The simulation in this work uses the

later set of the grids, the source model, and the survey data available at NTHMP repository of benchmark problems.

The computational domain used to simulate the 1993 Okushiri tsunami and the initial sea surface deformation are shown in the left pane in Fig. 23. The computations at a resolution of 30 s of the Great arc were refined with nested grids spaced at 10 arc-sec, 2 arc-sec (circling Okushiri island), 15 m (enclosing Aonae area), and 6 m (enclosing Monai valley). The grids contours are pictured in Fig. 23. In the two outer level grids, a vertical wall was imposed in 1 m deep water. In the 2 arc-sec grid around Okushiri, the wave higher than $h_{\min} = 0.5$ m was permitted to inundate the next dry cell, that is, to advance 40–60 m inland. In the two finest grids, the wave was permitted to inundate once it was higher than $h_{\min} = 0.1$ m. Friction coefficient in all grids was $n = 0.03$.

Locations of field measurements of the tsunami runup acquired by the Hokkaido Tsunami Survey

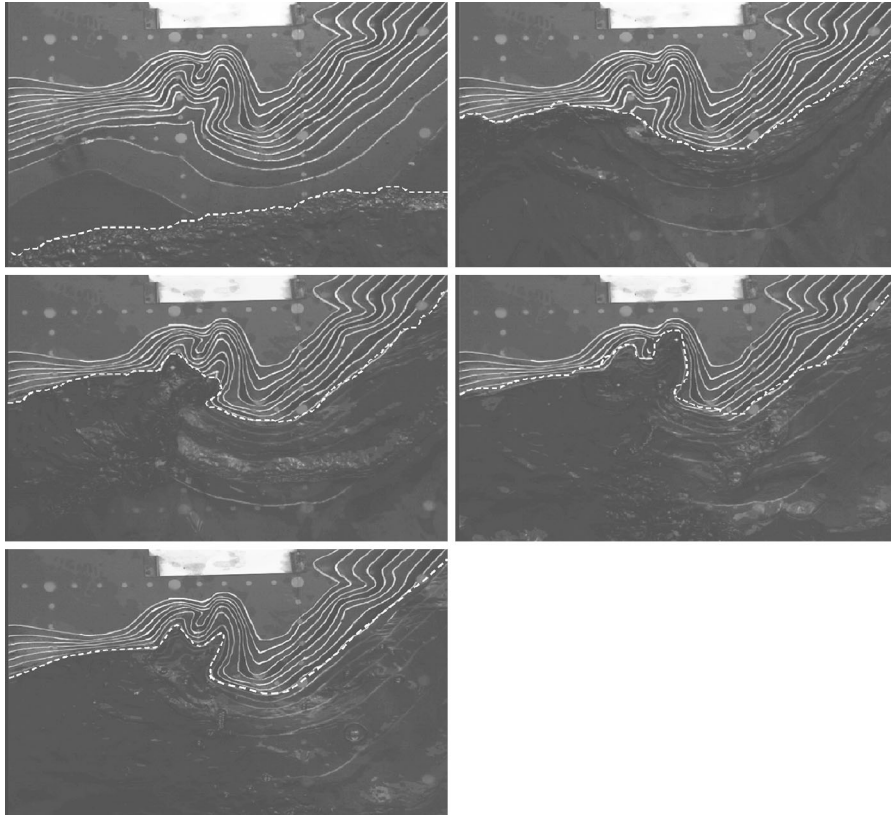


Figure 20
Five frames extracted from the video record of the lab experiment with 0.5 s interval

Group (HTSG 1993) are marked by dots in the right pane of the figure. Some of these locations appear to be in the sea, which reflects already mentioned inaccuracies in geophysical referencing. These data, totaling to 117 runup values with quality flags 1 and 2, had been extracted from the University of Tohoku publication (DCRC 1994) for the NTHMP 2011 workshop.

Figure 24 displays runup around Okushiri island computed with Cliffs and with MOST, compared to the survey data. Survey locations follow counterclockwise (in general) from the western boundary of the grid enclosing Aonae peninsular. Due to known errors in referencing, we did not attempt to extract a simulated runup value at a point closest to the observation point according to its coordinates. Instead, the maximum runup value within a 300×300 m box around the anticipated closest observation location was used. Figure 25 shows measured tsunami runup and that computed with Cliffs around Aonae peninsular.

Maximum modeled runup height obtained at Hamatsumae was 12 m (reported up to 13.2 m), in Monai valley 20 m (reported up to 31.7 m), and in Aonae 12.2 m (reported 12.4 m). It's common among numerical models to under-estimate runup at Monai valley. The reasons behind this are discussed in NICOLSKY *et al.* (2011). Overall, the simulated runup reproduced the measurements location-wise fairly well. However, Cliffs (similar to many other models) did not capture extreme runup east of Hamatsunami, while MOST did, even with the coarser 2 s grid. MOST also computed about 1 m higher runup in some other areas, including Monai.

6.5. Discussion of MOST and Cliffs Inundation Computations

Among four benchmarks, MOST and Cliffs results are very close in two tests, and somewhat different in the other two. A possible reason for the

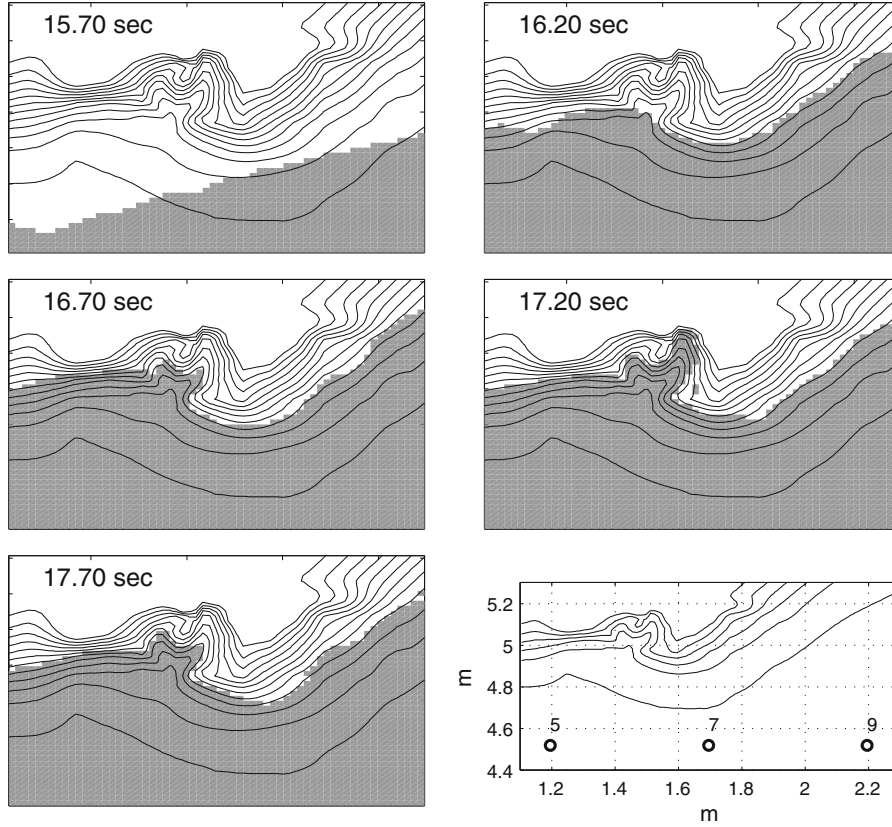


Figure 21

Five snapshots of simulated water height distribution with 0.5 s interval. *Bottom right* location of the gages 5, 7, 9

observed differences is a very different regime of generation of water by each inundation algorithm.

A significant part of the Aonae grid constitutes repeatedly inundated land. The summed-up instant sea surface displacements and water depth over inundated land in all grid cells represent an instant total volume of excess water in the grid divided by the cell area, further referred to as the total excess elevation. For this experiment, tsunami propagation from the source earthquake to Okushiri island in the three upper level grids had been done with Cliffs, while computations in the innermost level grid around Aonae peninsular were performed with either MOST or Cliffs, under identical boundary input. Since the amount of water propagating into the Aonae grid is the same in computations with MOST and Cliffs, one should not expect significant differences between the two models in the total excess

elevation in the grid at any moment. The difference between instant total elevations computed with MOST and with Cliffs, as a function of time, is shown in Fig. 26. Also shown is the total flood depth (summed-up depth in flooded land cells) computed with each model. Contradictory to the expectations, MOST, in general, has more water in the grid than Cliffs. The difference between the models in the amount of the excess water appears precisely when inundation starts, and is overall correlated with repeating inundation events.

The inundation algorithm of either model creates and destroys water. In Cliffs, water is added on runoff in step (b) (see Sect. 5) at a uniform rate $h_{\min} = 0.1$ m of water column per a cell per an inundation event. Water is removed on rundown in step (a), h_{\min} or less per a cell being dried out. Water is also removed in relatively few cells on runoff in step (e). Amount of

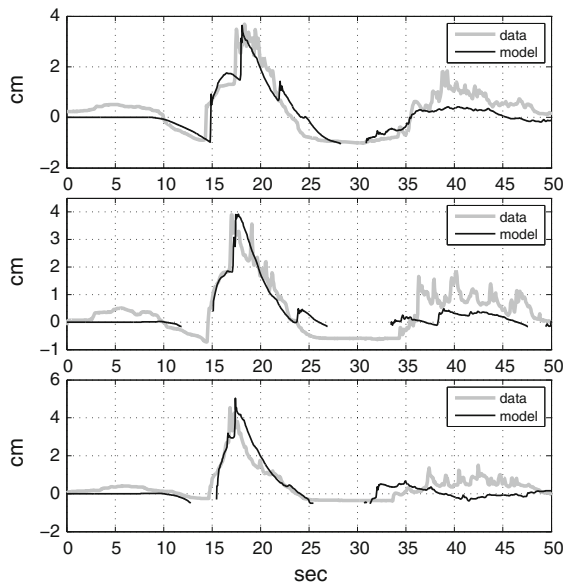


Figure 22
Modeled and recorded water level time histories at the gages 5, 7, 9
(top to bottom)

water grid-wide added/destroyed in each inundation step and altogether was summed-up in each solution cycle. A solution cycle computes wave evolution through one time step $\Delta t = 0.5$ s in every row and every column of the 220×280 Aonae grid. The resulting water amounts and the net amount added by Cliffs from the start of the simulation vs a cycle time are plotted in Fig. 27. According to NOAA's standards, a tsunami model conserves mass if it gains or loses less than 5 % of initially displaced water by the end of the computations, i.e. when the initial wave is entirely reflected and offshore (SYNOLAKIS *et al.* 2007). For comparison, after all runup/rundown activity in the Aonae simulation, Cliffs removed $400 \times 15 \times 15 \text{ m}^3$ of water, which constitutes 0.001% of the initially displaced water in the tsunami origin.

At the same time, the amount of water being added/removed by Cliffs is insufficient to account for the difference between MOST and Cliffs in the amount of excess water in the domain. Therefore, this

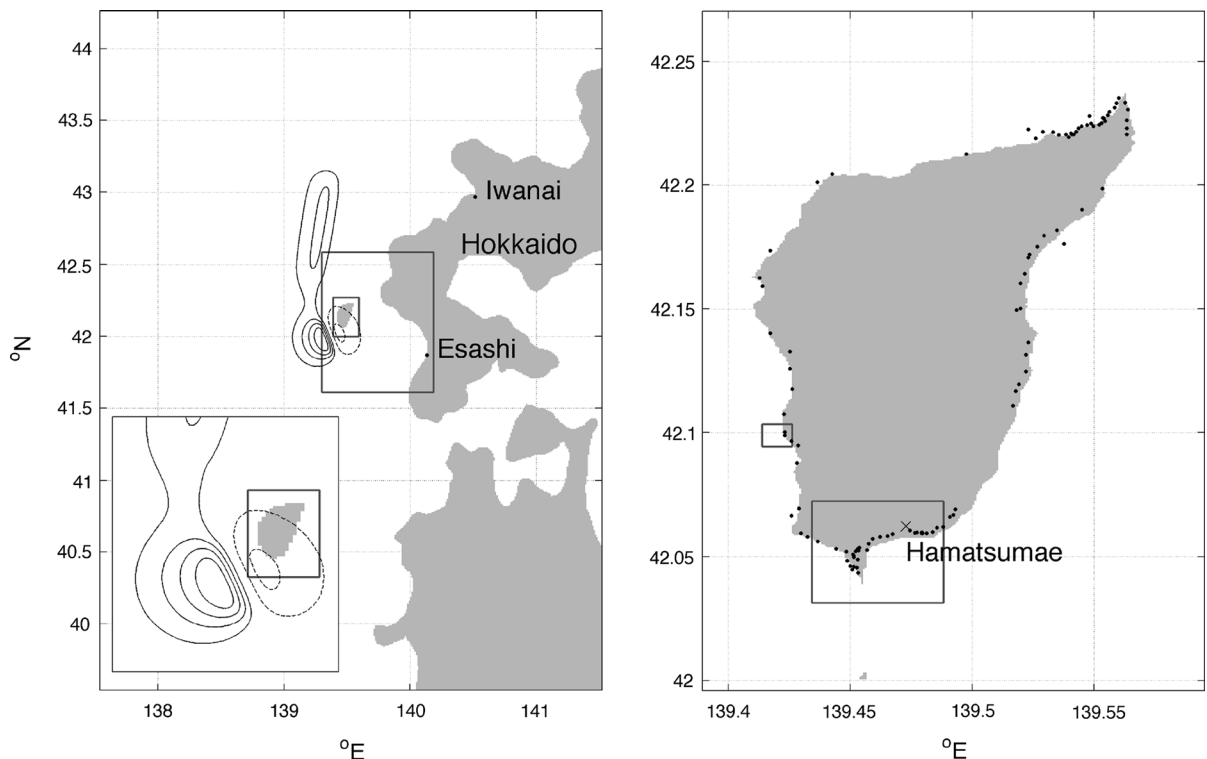


Figure 23

Left computational domain used to simulate the 1993 Hokkaido tsunami with contours of the two nested grids; initial sea surface deformation with contour lines at $-1, -0.5, 1, 2, 3, 4$ m levels, subsidence contours are shown with *dashed lines*, uplift with *solid lines*. The deformation area near Okushiri is zoomed-in in the bottom left corner. Right 3-d nesting level grid around Okushiri island with contours of the 4-th level grids around Monai and Aonae; locations of field measurements

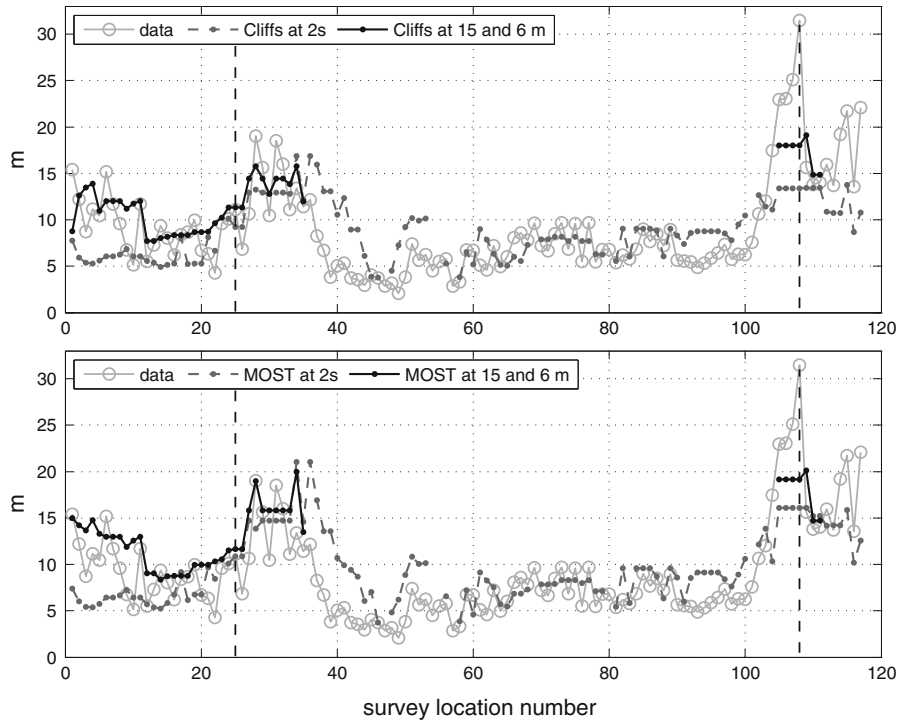


Figure 24

Runup around Okushiri island computed in the island-wide grid at 2 s resolution (*dark gray dashed*) and refined with higher resolution grids around Aonae and Monai (*black*), and the survey data (*gray circles*), per observation location. *Dashed vertical lines* mark locations near Hamatsumae (*left*) and Monai (*right*). Computations with Cliffs (*top pane*) and MOST (*lower pane*)

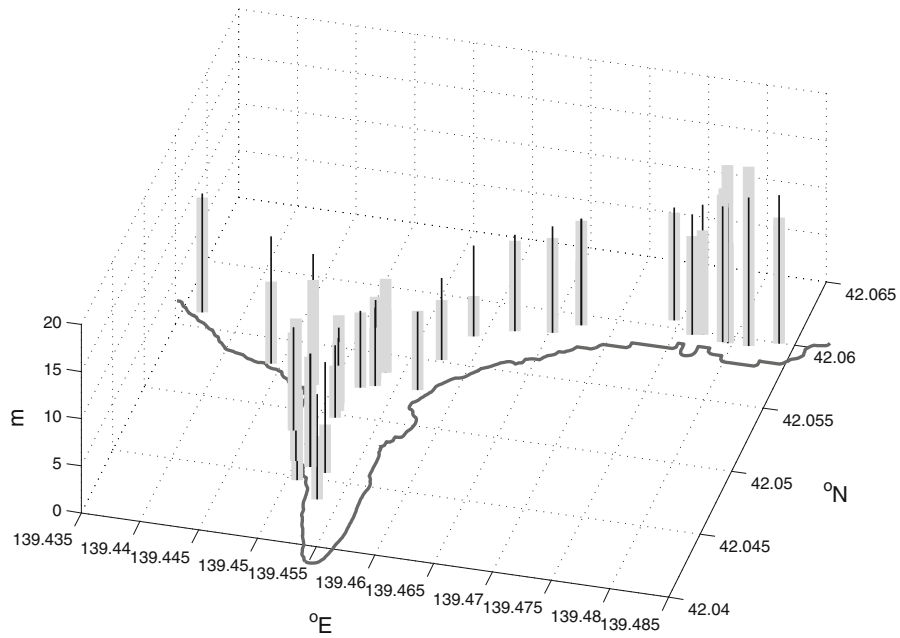


Figure 25

Runup around Aonae peninsular computed with Cliffs (*black thin vertical bars*) and the survey data (*gray thick bars*), per observation location

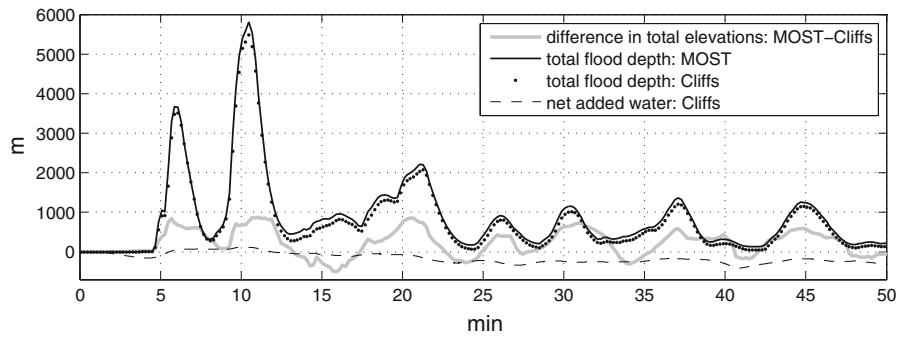


Figure 26

Difference between total excess elevations in the Aonae grid computed with MOST and with Cliffs; total flood depth computed with MOST and with Cliffs; and the amount of water (in terms of water column height) added by Cliffs inundation algorithm over simulation life, functions of time

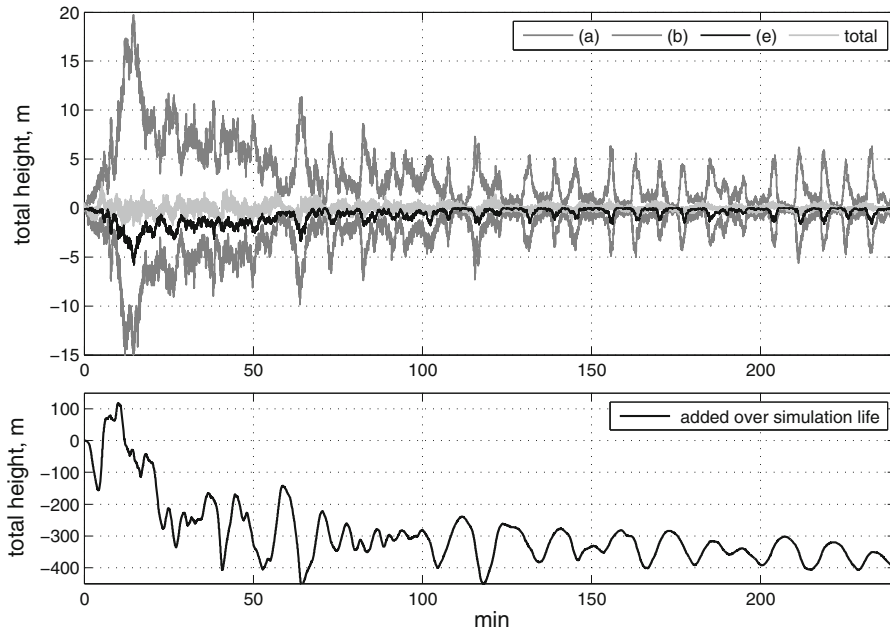


Figure 27

Top the total height of water added by Cliffs in steps (a) (negative), (b) (positive), (e) (negative), and altogether, in one cycle of computations in the Aonae grid; *bottom* amount of water added by Cliffs inundation algorithm over simulation life

difference should be attributed to water created by the MOST inundation algorithm. By the mere amount of this water, inundation computations in MOST are affected by water generation on a shoreline to a greater degree than those in Cliffs. MOST changes amount of water and momentum both explicitly—by drying out cells filled below a threshold, and in much greater amounts implicitly—by manipulating extent

of wet cells on a shoreline. The latter makes it difficult to directly evaluate the resulting change. An amount of water created/destroyed in each shoreline cell by manipulating the cell size is comparable with an amount of water already in the cell, and it is greater the higher the wave, which might facilitate obtaining extreme runups (Okushiri benchmark) or obstruct a runup (the first benchmark).

7. Summary

The MOST model adapted by NOAA for tsunami forecasting operations is praised for its computational efficiency, associated with the use of splitting technique. However, splitting of the computations between x and y directions might result in underestimating the wave reflected by a shoreline, unless the shoreline is aligned with a coordinate axis. Slight modification to the reflective boundary conditions in MOST, equivalent to a half-node re-positioning of the reflecting wall within a cell, caused an appreciable difference in the results in some situations. This is demonstrated with simulations of the Tohoku-2011 tsunami from the source earthquake to Monterey Bay, California, and in southeast Alaska, followed by comparison with tide gage records. In the first case, the better representation of later waves (those reflected from the coasts) by the modified model in a Pacific-wide simulation resulted in twice as long match between simulated and observed tsunami time histories at Monterey gage. In the second case, the modified model was able to propagate the tsunami wave and approach gage records at locations within narrow channels (Juneau, Ketchikan), to where MOST had difficulty propagating the wave. It has been shown, that the model's sensitivity to formulating reflective boundary conditions is a consequence of approaching a 2D problem as a sequence of 1D problems.

The modification was extended to include runup computations. The resulting inundation algorithm (Cliffs) provides a coding-friendly wet-dry interface, to complement the known propagation algorithm. Cliffs is approximately 10 % more efficient computationally than the MOST algorithm, and is implemented precisely as it is described. Cliffs has been tested with the complete set of NTHMP-adapted benchmark tests focused on inundation. The solutions are compared to the MOST solutions obtained with the version of the MOST model benchmarked for NTHMP in 2011. In two tests, Cliffs and MOST results are very close, and in another two tests, the results are somewhat different. Very different regimes of generation/disposal of water and momentum by Cliffs and MOST inundation algorithms, which supposedly affected the benchmarking results, have been discussed.

Acknowledgments

Author thanks tsunami modelers—participants of the 2011 NTHMP Model Benchmarking Workshop—for collecting and systemizing data used in this work for testing the inundation algorithm. In particular, bathymetric and land survey data for the Okushiri tsunami have been collected and refined by Dmitry Nicolsky and Frank Gonzalez. The analytical solution to the non-breaking solitary wave runup onto the sloping beach shown in Figs. 13 and 14, and the video frames of the wave-tank experiment with a model of Monai area shown in Figure 20, are courtesy of Dmitry Nicolsky. Author acknowledges NOAA/NOS for providing gauge records, and NOAA/NGDC for providing bathymetry data.

REFERENCES

- BRIGGS, M. J., SYNOLAKIS, C. E., HARKINS, G. S., and GREEN, D. R. (1995), *Laboratory experiments of tsunami runup on a circular island*. Pure Appl. Geophys., 144, 3/4, 569–593.
- BURWELL, D., TOLKOVA, E., and CHAWLA, A. (2007), *Diffusion and Dispersion Characterization of a Numerical Tsunami Model*. Ocean Model., 19 (1–2), 10–30. doi:10.1016/j.ocemod.2007.05.003.
- BURWELL, D., TOLKOVA, E. (2008). Curvilinear version of the MOST model with application to the coast-wide tsunami forecast, Part II. NOAA Tech. Memo. OAR PMEL-142, 28 pp.
- DISASTER CONTROL RESEARCH CENTER. Tsunami Engineering Technical Report No. 11, Tohoku University, March 1994.
- GONZALEZ F.I., LEVEQUE R.J., CHAMBERLAIN P., HIRAI B., VARKOVITZKY J., and GEORGE D.L., GeoClaw Model, In: [NTHMP] National Tsunami Hazard Mitigation Program. July 2012. Proceedings and Results of the 2011 NTHMP Model Benchmarking Workshop. Boulder: U.S. Department of Commerce/NOAA/NTHMP; NOAA Special Report. 436 p.
- HOKKAIDO TSUNAMI SURVEY GROUP (1993), Tsunami devastates Japanese coastal region. Eos Trans. Am. Geophys. Union, 74(37), 417–432.
- IMAMURA F., Tsunami Modeling: Calculating Inundation and Hazard Maps. In: The Sea, 15. Tsunamis. Ed: BERNARD E. and ROBINSON A. Harvard University Press, Cambridge, MA, London, England 2009.
- LEVEQUE, R.J., Finite volume methods for hyperbolic problems. Cambridge University Press, UK 2002.
- LI, Y., and RAICHLEN, F. (2002), *Non-breaking and breaking solitary wave run-up*. J. Fluid Mech., 456, 295–318.
- LIU, P.L.-F., CHO, Y.-S., BRIGGS, M., KANOGLU, U., and SYNOLAKIS, C. (1995), *Runup of solitary waves on a circular island*. Journal of Fluid Mech. 302, 259–285.
- LIU, P.L.-F., YEH, H., and SYNOLAKIS C. (2008), *Advanced Numerical Models for Simulating Tsunami Waves and Runup*. Advances in Coastal and Ocean Engineering, 10, 223–230.

- NICOLSKY, D.J., SULEIMANI, E.N., and HANSEN, R.A. (2011), *Validation and verification of a numerical model for tsunami propagation and runup*. Pure Appl. Geophys. 168, 1199–1222.
- [NTHMP] NATIONAL TSUNAMI HAZARD MITIGATION PROGRAM, July 2012. Proceedings and Results of the 2011 NTHMP Model Benchmarking Workshop. Boulder: U.S. Department of Commerce/NOAA/NTHMP; NOAA Special Report. 436 p.
- ROEBER, V., CHEUNG, K.F., and KOBAYASHI, M.H. (2010), *Shock-capturing Boussinesq-type model for nearshore wave processes*. Coastal Engineering 57, 407–423.
- SHI, F., KIRBY, J.T., HARRIS, J.C., GEIMAN, J.D., GRILLI, S.T. (2012), *A high-order adaptive time-stepping TVD solver for Boussinesq modeling of breaking waves and coastal inundation*. Ocean Modelling, 43–44, 36–51.
- STRANG, G. (1968), *On the construction and comparison of difference schemes*. SIAM Journal on Numerical Analysis, 5(3), 506–517.
- SYNOLAKIS, C.E. (1987), *The runup of solitary waves*. J. Fluid Mech., 185, 523–545.
- SYNOLAKIS, C.E., BERNARD, E.N., TITOV, V.V., KANOGLU, U., and GONZALEZ, F.I. (2007), Standards, criteria, and procedures for NOAA evaluation of tsunami numerical models. NOAA Tech. Memo. OAR PMEL-135, NTIS: PB2007-109601, NOAA/Pacific Marine Environmental Laboratory, Seattle, WA, 55 pp.
- TANG, L., TITOV, V. V., and CHAMBERLIN, C. D. (2009), *Development, testing, and applications of site-specific tsunami inundation models for real-time forecasting*, J. Geophys. Res., 114, C12025, doi:[10.1029/2009JC005476](https://doi.org/10.1029/2009JC005476).
- TANG L., TITOV, V.V., BERNARD, E., WEI, Y., CHAMBERLIN, C., NEWMAN, J.C., MOFJELD, H., ARCAS, D., EBLE, M., MOORE, C., USLU, B., PELLIS, C., SPILLANE, M.C., WRIGHT, L.M., and GICA, E. (2012), *Direct energy estimation of the 2011 Japan tsunami using deep-ocean pressure measurements*, J. Geophys. Res., VOL. 117, C08008, doi:[10.1029/2011JC007635](https://doi.org/10.1029/2011JC007635).
- TAKAHASHI, T. (1996), Benchmark problem 4: the 1993 Okushiri tsunami - Data, conditions and phenomena. In Long-Wave Runup Models, World Scientific, 384–403.
- TITOV, V. V., and SYNOLAKIS, C. E. (1995), *Modeling of breaking and nonbreaking long-wave evolution and runup using VTCS-2*, J. Waterw., Port, Coastal, Ocean Eng., 121(6), 308–316.
- TITOV, V., and GONZALEZ F.I. (1997), Implementation and testing of the Method of Splitting Tsunami (MOST) model. NOAA Tech. Memo. ERL PMEL-112 (PB98-122773), NOAA/Pacific Marine Environmental Laboratory, Seattle, WA, 11 pp.
- TITOV, V. V., and SYNOLAKIS, C. E. (1998), *Numerical modeling of tidal wave runup*, J. Waterw., Port, Coastal, Ocean Eng., 124(4), 157–171.
- TITOV V. V., GONZALEZ, F. I., BERNARD, E. N., EBLE, M. C., MOFJELD, H. O., NEWMAN, J. C., and VENTURATO, A. J. (2005), *Real - Time Tsunami Forecasting: Challenges and Solutions*, Natural Hazards, 35:41–58.
- TOLKOVA, E. (2012), MOST (Method of Splitting Tsunamis) Numerical Model. In: [NTHMP] National Tsunami Hazard Mitigation Program. Proceedings and Results of the 2011 NTHMP Model Benchmarking Workshop. Boulder: U.S. Department of Commerce/NOAA/NTHMP; NOAA Special Report. 436 p.
- VAN DORN, W. G. (1984), *Some tsunami characteristics deducible from tide records*, J. Phys. Oceanogr., 14, 353–363.
- WEI, Y., MAO, X.-Z., and CCHEUNG, K.F. (2006), *Well-Balanced Finite-Volume Model for Long-Wave Runup*. Journal of Waterway, Port, Coastal, and Ocean Engineering, 132 (2), 114–124.

(Received November 5, 2013, revised March 3, 2014, accepted March 4, 2014)